2010-06

Viability of using diamond field emitter array cathodes in free electron lasers

Hallock, Samuel H.

Monterey, California. Naval Postgraduate School

NAVAL POSTGRADUATE SCHOOL

MONTEREY, CALIFORNIA

THESIS

VIABILITY OF USING DIAMOND FIELD EMITTER ARRAY CATHODES IN FREE ELECTRON LASERS

by

Samuel H. Hallock

June 2010

Thesis Co-Advisors: John Lewellen
Richard Swent

Approved for public release; distribution is unlimited

THIS PAGE INTENTIONALLY LEFT BLANK

REPORT DOCUMENTATION PAGE		Form Approved OMB No. 0704-0188

1. AGENCY USE ONLY *(Leave blank)*	2. REPORT DATE	3. REPORT TYPE AND DATES COVERED
	June 2010	Master's Thesis

4. TITLE AND SUBTITLE
Viability of Using Diamond Field Emitter Array Cathodes in Free Electron Lasers

5. FUNDING NUMBERS

6. AUTHOR(S) Samuel H. Hallock

7. PERFORMING ORGANIZATION NAME(S) AND ADDRESS(ES)
Naval Postgraduate School
Monterey, CA 93943-5000

8. PERFORMING ORGANIZATION REPORT NUMBER

9. SPONSORING /MONITORING AGENCY NAME(S) AND ADDRESS(ES)
N/A

10. SPONSORING/MONITORING AGENCY REPORT NUMBER

11. SUPPLEMENTARY NOTES The views expressed in this thesis are those of the author and do not reflect the official policy or position of the Department of Defense or the U.S. Government. IRB Protocol number _____.

12a. DISTRIBUTION / AVAILABILITY STATEMENT	12b. DISTRIBUTION CODE
Approved for public release; distribution is unlimited	A

13. ABSTRACT (maximum 200 words)

Developing free electron lasers (FEL) for shipboard use is of great interest to the United States Navy. This thesis gains insight, through simulation and design, into the potential use of diamond tipped field emitter array (DFEA) cathodes within the FEL system. Based on the operational requirements for a DFEA, a cathode-anode geometry was designed. Simulations were run on this design to determine if this configuration will work in a high voltage. Additionally, a cathode test cell was constructed to carry out follow on experiments. Finally, recommendations are made for future experimentation using the cathode test cell based on the results of this thesis.

14. SUBJECT TERMS	15. NUMBER OF PAGES
Free Electron Lasers, Field Emitter Arrays, Cathode Test Cell, FEL, Diamond Field Emitter Array, Cathode	89
	16. PRICE CODE

17. SECURITY CLASSIFICATION OF REPORT	18. SECURITY CLASSIFICATION OF THIS PAGE	19. SECURITY CLASSIFICATION OF ABSTRACT	20. LIMITATION OF ABSTRACT
Unclassified	Unclassified	Unclassified	UU

NSN 7540-01-280-5500 Standard Form 298 (Rev. 2-89)
Prescribed by ANSI Std. 239-18

THIS PAGE INTENTIONALLY LEFT BLANK

Approved for public release; distribution is unlimited

VIABILITY OF USING DIAMOND FIELD EMITTER ARRAY CATHODES IN FREE ELECTRON LASERS

Samuel H. Hallock
Lieutenant, United States Navy
B.S., United States Naval Academy, 2001
M.E.M., Old Dominion University, 2006

Submitted in partial fulfillment of the
requirements for the degree of

MASTER OF SCIENCE IN APPLIED PHYSICS

from the

NAVAL POSTGRADUATE SCHOOL
June 2010

Author: Samuel H. Hallock

Approved by: John Lewellen
Thesis Advisor

Richard Swent
Co-Advisor

Andres Larraza
Chairman, Department of Physics

THIS PAGE INTENTIONALLY LEFT BLANK

ABSTRACT

Developing free electron lasers (FEL) for shipboard use is of great interest to the United States Navy. This thesis gains insight, through simulation and design, into the potential use of diamond tipped field emitter array (DFEA) cathodes within the FEL system. Based on the operational requirements for a DFEA, a cathode-anode geometry was designed. Simulations were run on this design to determine if this configuration will work in a high voltage. Additionally, a cathode test cell was constructed to carry out follow on experiments. Finally, recommendations are made for future experimentation using the cathode test cell based on the results of this thesis.

THIS PAGE INTENTIONALLY LEFT BLANK

TABLE OF CONTENTS

THIS PAGE INTENTIONALLY LEFT BLANK

LIST OF FIGURES

LIST OF ACRONYMS AND ABBREVIATIONS

FEL	Free Electron Laser
DFEA	Diamond Tipped Field Emitter Array
NPS	Naval Postgraduate School
INP	Innovative Navy Prototype
RF	Radio Frequency
LASER	Light Amplification by Simulated Emission of Radiation
COTS	Commercial Off-the-Shelf
SPIFFE	SPace charge and Integration of Forces for Electrons
MASER	Microwave Amplification by Stimulated Emission of Radiation

THIS PAGE INTENTIONALLY LEFT BLANK

ACKNOWLEDGMENTS

I would like to thank the Free Electron Laser Group at NPS for providing me with a wonderful opportunity to learn from a group of resident experts in this field. In particular, Dr. William Colson and Dr. Blau, for their continued efforts in teaching me the fundamentals of the FEL system, and letting me be a part of this group. I would also like to thank my thesis advisors, Dr. John Lewellen and Dr. Richard Swent, whose expert guidance and tutelage have been instrumental in my success here at NPS.

THIS PAGE INTENTIONALLY LEFT BLANK

I. INTRODUCTION

This thesis focuses on simulating field emission cathodes for future use in free electron lasers (FELs). However, it is useful to understand a brief history of directed energy and the benefits that FELs provide over other types of lasers.

The concept of directed energy began nearly a century ago, when Einstein's work on re-deriving Plank's equations set the groundwork for the maser and later the laser. In 1953, Charles H. Townes successfully demonstrated the maser, which produced coherent electromagnetic waves. The maser was then used as the basis for creating the laser, which produces coherent optical waves. Along with Townes, Gordon Gould and Lawrence Goldmuntz both hypothesized that generating a coherent beam of light was indeed possible. Although Townes and Gould were working on creating a functional laser, it was Theodore Maiman who was the first to build and demonstrate a laser when his pulsed ruby laser came online. Maiman's success was a sign of future growth in this exciting new field, and of the multitude of functions for which a laser could be used. Unfortunately for Maiman, his design was only able to produce very low power, limited by the physical properties of the ruby oscillator-amplifiers that were necessary. This problem ended up giving rise to the use of gas lasers (which had been suggested by Gould). These early gas lasers were the first true high-energy lasers; however, they, too, were limited in the amount of power they were able to produce. The next iteration proved to be chemical lasers (circa

1973), which were more powerful and much larger in size. It was also in the mid-1970s that free electron lasers first came into existence.

Although chemical lasers were indeed powerful, they experienced problems when trying to shoot down targets traveling through the atmosphere. The lasers were heating the air, which resulted in thermal blooming, and this in turn caused the lasers' energy to spread out and reduce the power density that was delivered directly to the target. The laser craze began to cool somewhat by the early 1980s, but this slight cooling was soon to change when the "Star Wars" era began. The "Star Wars" era concept focused on using space-based lasers (capable of shooting roughly 1000 times) that would be used to shoot down ballistic nuclear missiles and act as a shield against potential nuclear attack. This renewed interest in lasers as a ballistic missile defense greatly increased the funding that went into laser research. Unfortunately, when the Soviet Union collapsed the need for a "Star Wars" defense system was no longer a high priority. As a result, the Pentagon stopped most of its research on land-based free electron lasers and instead focused its efforts on airborne chemical lasers. These systems were severely limited by the amount of chemicals that must be carried in order for the lasers to operate. Recently, the U.S. Navy began intensive efforts to develop a shipboard FELs.

Free electron lasers (FELs), which have been around since the 1970s, are incredibly versatile. They use electrons, not bound within any medium, to create laser light and, as such, they are not limited by any of the

lasing medium problems that are encountered by solid-state, gas, or chemical lasers. Another benefit of FELs is their inherent flexibility. By varying just a few system parameters the overall output (both power and wavelength) of the system can be varied without having to alter the system construction.

High-power FELs can be both very efficient as well as reliable. These systems have been shown to operate for several weeks continuously and, at weapons-class power levels, should have efficiencies up to 20% wall plug. However, such positive attributes do come with the downside of very large size and cost. Currently, there are several initiatives to reduce both of these drawbacks in order to produce a viable sized and priced system for shipboard use [1].

Chapter II discusses the components of a free electron laser in order to provide an understanding of how all the pieces of the FEL fit together. Chapter III discusses the theory behind free electron lasers in order to illuminate how electrons can ultimately be used to generate a coherent beam of light, and the benefits provided by using field emission cathodes. In Chapter IV, the theory and mechanisms behind field emission cathodes are examined, as well as the forces that act on the electrons while they travel within the cathode itself.

Chapter V discusses the design and construction of a cathode test cell, to include the design parameters and the computer simulations used in testing various cathode-anode geometries. No experiment would be complete without some educated guesses upon which to compare the observed

results. Chapter VI follows the simulations that were carried out in order to predict the experimental outcome. Chapter VII discusses and compares the results of the simulation and makes recommendations for future tests.

II. FREE ELECTRON LASER SYSTEM

In this section, the FEL system is described, starting from where the electrons are generated, following them as they travel through the FEL, and describing the components that they encounter.

FELs have two major types of configurations: amplifier FELs and oscillator FELs. Both of these configurations are shown in Figure 1. The main difference between these two configurations is how energy in the form of light is extracted from the FEL. In amplifier configurations a seed laser is amplified over one pass of the undulator; in an oscillator a resonator is used in conjunction with several electron passes to generate the output laser beam. Figure 1 shows both paths on the same machine. Granted, not all FELs have this configuration; however, this is useful in visualizing both systems. This introduction deals primarily with the oscillator design; however, in principle field emitter cathodes could be used with either type of FEL.

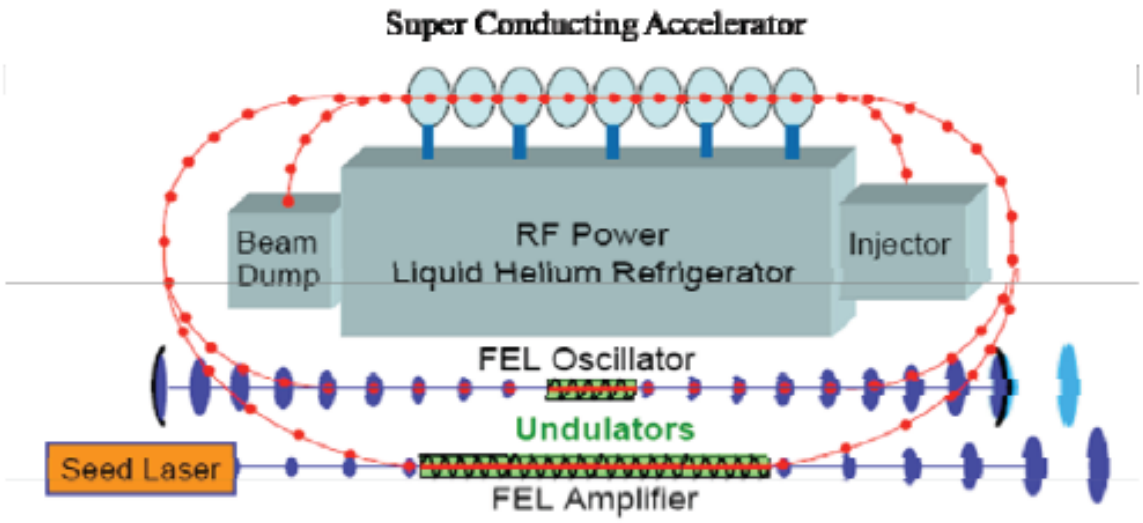

Figure 1. The Free Electron Laser System (From [1])

A. THE INJECTOR

The injector is the start of all FELs. It is here that the initial electron beam is produced. The injector uses a cathode to produce a steady beam of electrons that are relatively close in energy. Cathodes produce electrons in one of three main ways: photoelectric effect, thermionic emission, or field emission [2]. For photoelectric effect cathodes, a drive laser illuminates a cathode and, provided the energy of the photons shining on the cathode is greater then the work function of the cathode, electrons are liberated. For thermionic cathodes, the cathode is heated until the temperature of the electrons exceeds the cathode's work function, at which point electrons are produced. Lastly (and most importantly for this thesis) are field emission cathodes. These cathodes rely upon geometry to create locations of high electric fields (for this thesis the pyramid shaped tips of diamond substrate). When these cathodes are in the presence of an electric field the "points or tips" enhance the electric field to a

level at which electrons are directly "sucked out" of the field emitter tip. This phenomenon is discussed in greater detail in Chapter IV, section A.

The injector design (including cathode choice) greatly affects the overall FEL system performance. The goal is to produce an electron beam that is of the highest beam quality and as mono-energetic as possible. This will help the rest of the FEL system to radiate more efficiently and increase the overall power that can be extracted from the FEL.

B. ACCELERATOR

The next component encountered by the electron beam is the superconducting electron accelerator. For this thesis, we are going to focus on RF accelerators, as that is the type to be used in the Navy INP. The accelerator consists of a series of metal cavities that have external RF power supplied. By applying power in this fashion, strong electromagnetic fields are generated within the cavities. These fields are alternating in nature, and this property is controlled such that when the electrons enter the accelerator, they gain energy over the course of the accelerator and, thus, greatly increase in voltage. The electrons leave the accelerator at very high relativistic voltages, which is crucial to the generation of a laser from electrons.

C. CONTROLLING DIAGONOSTICS

Since our proposed FEL design will be re-circulating in nature, it is important to note that there will be controlling mechanisms through the system to focus and

guide the electron beam. After the electron beam exits the accelerator, it will enter into a series of electromagnets that will be used to bend the beam's path and direct it into the undulator. Here again, the overall beam quality comes into play. Beams with higher beam quality will be able to maintain more of their energy in a centrally focused manner and, as such, a better overall beam will then enter into the undulator [1].

D. THE UNDULATOR

The undulator is made up of a series of powerful rare-earth magnets with alternating poles. This arrangement produces an alternating transverse magnetic field that occurs along the beam path. The transverse magnetic field acts to periodically deflect the electron, creating a side-to-side "wiggling" motion. It is this "wiggling" motion that is central to the formation of a laser from a relativistic electron beam, as it allows for energy transfer from the electron beam to the light wave. This interaction is discussed in greater detail in Chapter III. There are two major configurations for undulators: helical and linear. Figure 2 shows a linear undulator.

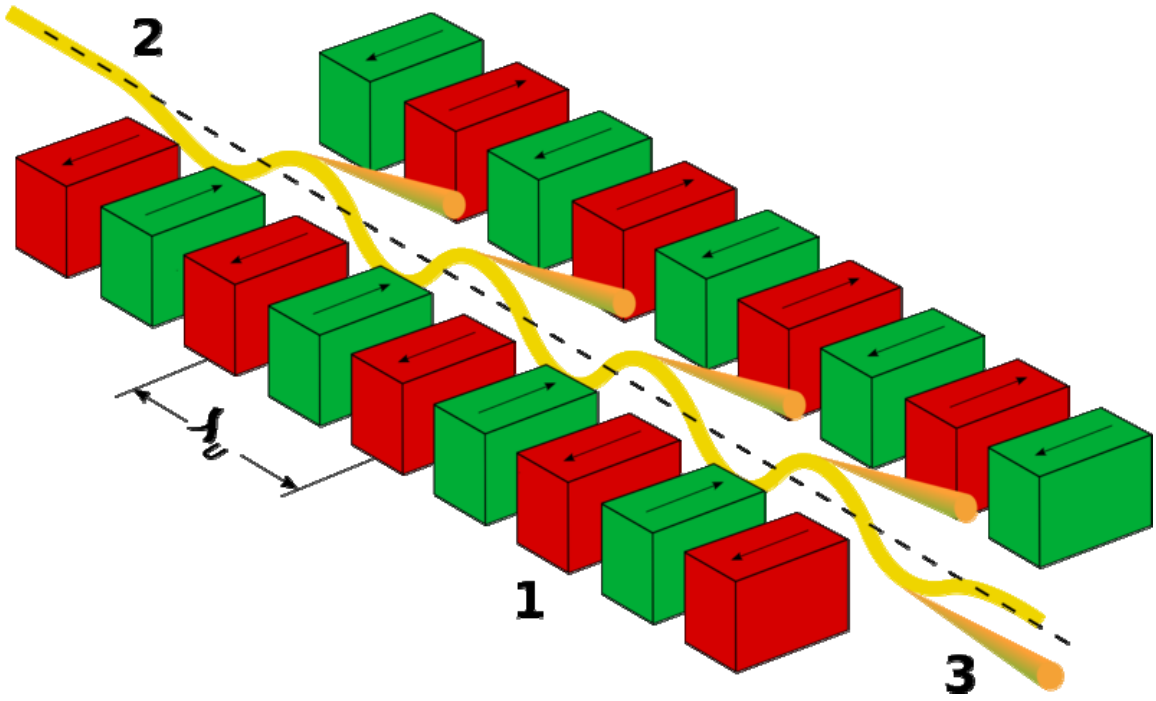

Figure 2. Linear undulator with the electron beam represented by the sinusoidal yellow line (From [2])

E. THE RESONATOR AND OPTICS

The undulator is contained within a resonator cavity. This cavity is evacuated and contains two mirrors (one at each end of the cavity). One of the mirrors is completely reflective, while the other is partially transmissive. It is this transmissivity that allows for laser energy to leave the cavity and then be utilized. In the oscillator configuration, the initial source of light is spontaneous emission. This light then proceeds to be reflected between the two mirrors and interacts with the electron beam over several passes through the system, to further coherently amplify the light beam. The final result is a coherent beam of high-energy light: a laser beam [1].

The resonator cavity itself stores energy and as a result cavities with short Raleigh lengths are utilized. A short Rayleigh length cavity serves to focus the light beam in the center of the cavity (where there are no optical components) to about 1mm in radius and in turn it defocuses the beam at the mirrors so that the beam's radius is roughly 3cm. This spreads out the optical energy over a larger area at the mirror surfaces and allows for a longer useful life of the resonator mirrors. Additionally, the short Rayleigh length allows the system to be constructed in a manner that does not require a huge distance between the mirrors.

F. BEAM TERMINATION

The FEL that is currently being developed for potential shipboard use by the Navy is a very high-power system. Extracting energy from the high-power electron beam for purposes of producing the laser only reduces the electron beam power by a few percent. A shipboard FEL must reclaim this power, both to increase efficiency of the system and to reduce the amount of radiation that is emitted by material interactions with the electron beam as it loses energy. To accomplish this, the accelerator system re-circulates the electron beam through the accelerator but this time out of phase with the RF field. This results in the electron beam giving up energy. This now far less energetic beam is directed into a beam dump where it essentially strikes, usually at a grazing incident, into a copper plate (or some other material). Since the beam has had its energy greatly reduced by passing through the accelerator out of phase, the resulting

material interaction that occurs in the beam dump does not produce neutron radiation and minimizes X-ray generation. This in turn reduces the amount of shielding that would be required for shipboard use [1].

THIS PAGE INTENTIONALLY LEFT BLANK

III. FREE ELECTRON LASER THEORY

Free electron lasers operate in a manner that is quite different from conventional lasers. In fact the name itself gives rise to the critical difference between the two types of lasers. In conventional lasers there is some lasing medium (solid, liquid, or gas) that contains the electrons which are excited to produce coherent light. In an FEL the electrons are never contained in any medium, rather they are extracted from the cathode into free space and then further accelerated (in a vacuum) and controlled to produce coherent light. Since the electrons are not contained within a medium, there is no concern for medium heating as the laser beam becomes more powerful (which is a critical limitation of conventional lasers). Furthermore, since the electrons are not dependent upon a specific medium we can alter parameters of the system to create lasers of virtually any wavelength desired, thus adding a tremendous amount of flexibility over conventional lasers. This section will introduce and explain the fundamental principles that allow a laser to be generated from a beam of electrons [1].

The undulator is the heart of all free electron lasers as it is here where the interactions occur that produce light from electrons. That said, accelerator physics are vital to the free electron laser system but those interactions are not the focus of this discussion.

After electrons are accelerated to high relativistic speeds, they enter into the undulator, also referred to as a wiggler.

Before we start this discussion, it is helpful to define some parameters we use to describe the electrons motion. The first is the normalized time τ, where τ varies from 0 to 1 along the length of the undulator. Next, is the phase of the electron ζ, which is a measure of an electron's position relative to a beam of electrons contained within one optical wavelength λ. The phase velocity of an electron is represented by ν and measures the rate of change of ζ. The frequency of the optical field is $\omega = kc = \frac{2\pi c}{\lambda}$. The wavenumbers $k = \frac{2\pi}{\lambda}$ and $k_0 = \frac{2\pi}{\lambda_0}$ correspond to the optical wavelength λ of the photon beam, and the undulator period λ_0. $\beta_z = \frac{v_z}{c}$ is the normalized electron velocity along the axis of the undulator (the motion of the electron through the undulator occurs in the z direction). In our normalized coordinates:

$$\begin{aligned} &\tau = ct/L, \text{ where L is the length of the undulator} \\ &\varsigma = (k + k_0) * z - \omega t \\ &\nu = d\varsigma/d\tau = L[(k + k_0) * \beta_z - k] \end{aligned} \tag{3.1}$$

For this discussion, a helical undulator is used to simplify the mathematical expressions. Within the helical undulator the Lorentz force equations determine the motion of the electrons.

$$\begin{aligned} &\frac{d(\gamma\vec{\beta})}{dt} = -\frac{e}{mc}(\vec{E} + \vec{\beta} \times \vec{B}) \\ &\frac{d\gamma}{dt} = -\frac{e}{mc}\vec{\beta} \bullet \vec{E} \\ &\vec{B} = \vec{B}_{undulator} + \vec{B}_{optical} \end{aligned} \tag{3.2}$$

where $\vec{\beta} = \frac{\vec{v}}{c}$ is the normalized velocity, γ is the relativistic Lorentz factor $\left(\frac{1}{\sqrt{1 - v^2/c^2}} \right)$, e and m are the charge magnitude and mass of the electron. $\vec{E}$ is the optical electric field strength and $\vec{B}$ is the undulator's magnetic field strength. The magnetic field of the helical undulator is expressed as

$$\vec{B}_{Undulator} = B(\cos[k_0 z], \sin[k_0 z], 0) \tag{3.3}$$

Next, we define the electric and magnetic optical fields

$$\begin{aligned} \vec{E} &= E(\cos(\psi), -\sin(\psi), 0) \\ \vec{B}_{optical} &= E(\sin(\psi), \cos(\psi), 0) \\ \psi &= kz - \omega t + \varphi \end{aligned} \tag{3.4}$$

By substituting Equation (3.4) and (3.3) into Equation (3.2) we can determine the transverse motion of the electron (assuming $\beta_z \approx 1$)

$$\vec{\beta}_{\perp} = -\frac{K}{\gamma}(\cos[k_0 z], \sin[k_0 z], 0) \tag{3.5}$$

K is the undulator parameter and is a dimensionless measure of the field strength $K = \frac{eB_{rms}\lambda_0}{2\pi mc^2}$. The relativistic Lorentz factor provides a relationship between the electron's velocity and its energy to determine the normalized velocity in the z direction β_z [1].

$$\gamma^{-2} = 1 - \beta_{\perp}{}^2 - \beta_z{}^2 \Rightarrow \beta_z \approx 1 - (1 + K^2)/2\gamma^2 . \tag{3.6}$$

A. THE RESONANCE CONDITION (FEL EQUATION)

The resonance condition occurs where the energy transfer between the electrons and photons is optimized. The resonance condition, within the FEL, can be explained by relating it to a race between an electron and a photon. Consider an electron and a photon entering an undulator at the same time. When an electron enters the undulator at a speed of $\beta_z c$ it is subjected to magnetic fields that cause it to oscillate or wiggle transversely. It is this wiggling motion of the electron that causes optical radiation to be emitted. As the electron passes through one full undulator period, it slips behind a photon that entered the period at the same time. The difference in velocities of the photon and electron is

$$c(1-\beta_z) \tag{3.7}$$

The time for this race is

$$\Delta t = \lambda_0 / \beta_z c \tag{3.8}$$

Since the photon is moving faster than the electron, it wins the race by one optical wavelength. We can then calculate the winning distance (λ of the photon) by multiplying the difference in velocities by the time of the race.

$$\lambda = \lambda_0 (1+K^2)/2\gamma^2 \tag{3.9}$$

It is this equation (sometimes referred to as the FEL equation) that relates the optical wavelength (λ) generated by the FEL to other FEL parameters, such as beam energy (γ) and undulator period (λ_o) [1].

B. PENDULUM EQUATION

The pendulum equation is used to describe the microscopic electron dynamics of an FEL. The starting point for this derivation is the relativistic Lorentz force Equations (3.2). Initially the electron enters along the z-axis of the undulator

$$\vec{B} = B(\cos(k_0 z), \sin(k_0 z), 0) \quad (3.3) \text{ where } k_0 = \frac{2\pi}{\lambda_0}$$

The interaction between the electron beam and the electro-magnetic fields the beam encounters is described by the Lorentz force Equations.

$$\begin{aligned} \frac{d(\gamma\vec{\beta})}{dt} &= -\frac{e}{mc}(\vec{E} + \vec{\beta} \times \vec{B}), \\ \frac{d\gamma}{dt} &= -\frac{e}{mc}\vec{\beta} \bullet \vec{E}, \\ \gamma^{-2} &= 1 - \vec{\beta}^2 \end{aligned} \qquad (3.10)$$

Given the initial magnetic and electric fields an electron's motion in the undulator is determined by the undulator and laser fields. We can substitute these fields (3.3) and (3.4) into the Lorentz force Equations (3.2) to get

$$\begin{aligned} \frac{d(\gamma\vec{\beta}_\perp)}{dt} &= -\frac{e}{mc}[E(1-\beta_z)(\cos\psi, -\sin\psi, 0) + \beta_z B(-\sin k_0 z, \cos k_0 z, 0)] \quad \text{(a)} \\ \frac{d(\gamma\vec{\beta}_z)}{dt} &= -\frac{e}{mc}[E(\beta_x \cos\psi - \beta_y \sin\psi) + B(\beta_x \sin k_0 z - \beta_y \cos k_0 z)] \quad \text{(b)} \end{aligned} \qquad (3.11)$$

If we assume that $\beta_z \approx 1$ for relativistic electrons, and that the electron travels at approximately constant velocity $(z \approx ct,\ \mathrm{k}_0 z \approx \omega_0 t)$, then using the transverse motion in

the undulator defined in Equation (3.5) (with $K = \frac{cB}{mc^2 k_0}$), we can integrate these to get

$$\vec{x}_\perp \approx \frac{K}{\gamma}\frac{\lambda_0}{2\pi}(-\sin(\omega_0 t), \cos(\omega_0 t), 0) \tag{3.12}$$

and thus describe the wiggling motion of the electron.

The motion of the electron can be obtained by substituting the transverse motion into Equation (3.11b) as follows.

$$\dot{\gamma} = \frac{d\gamma}{dt} = -\frac{e}{mc}E(\beta_x \cos\psi - \beta_y \sin\psi) = \frac{eKE}{\gamma mc}\cos(\zeta + \phi) \tag{3.13}$$

Since the constants (k, k_0, ω) in the electron phase Equation are fixed, the ζ follows the electron's microscopic position. ζ allows us to plot the evolution of the electrons in phase space (a very useful tool for understanding FELs). Now, using the resonance condition $\lambda = \lambda_0(1-\beta_z)/\beta_z \approx \frac{\lambda_0(1+K^2)}{2\gamma^2}$ (3.9), where the phase velocity of the electron is defined as $\nu = \frac{d\zeta}{d\tau}$ ($\tau = ct/L$ which is dimensionless time, and N is the number of periods).

$$\dot{\nu} = 4\pi N \dot{\gamma}/\gamma \tag{3.14}$$

This result is combined this with (3.12) to get the FEL pendulum Equation:

$$\overset{\circ}{\nu} = \overset{\circ\circ}{\zeta} = |a|\cos(\zeta + \phi) \tag{3.15}$$

where $|a| = \frac{4\pi NeKLE}{\gamma^2 mc^2}$ is the dimensionless laser field amplitude.

Energy gain and extraction usually occur near resonance, and at this point ω is order of magnitude greater then ω_0. Since each electron has a different initial phase with $\sim 10^6$ electrons spaced over a 1 micron distance (typical values for our FEL), half of the electrons will move slightly faster than the other half within each laser wavelength, and this will create bunching of the electrons. And it is this electron bunch that radiates coherently. The electrons will go through energy changes and these changes will affect the electron position and consequently the electrons phase and phase velocities ν [1].

C. THE FREE ELECTRON LASER WAVE EQUATION

Starting from Maxwell's equations, we can obtain

$$(\vec{\nabla}^2 - \frac{1}{c^2}\frac{\partial^2}{\partial t^2})\vec{A}(\vec{x},t) = -\frac{4\pi}{c}\vec{J}_\perp(\vec{x},t)$$
$$\vec{A}(\vec{x},t) = \text{optical vector potential} \qquad (3.16)$$
$$\vec{J}_\perp(\vec{x},t) = \text{transverse current density}$$

The magnetic and electric fields of the laser can be derived from the vector potential. We assume that the field is slowly varying compared to the optical frequency ω=kc. Thus, the vector potential can be written as

$$\vec{A}(\vec{x},t) = \frac{E(\vec{x},t)}{k}\hat{\varepsilon}e^{i\alpha} \qquad (3.17)$$

Here $\alpha = kz - \omega t$ represent the "carrier wave", $\mathrm{E}=|\mathrm{E}|e^{i\theta}$ is the complex laser electric field, and $\hat{\varepsilon}$ is the laser field vector polarization. Since the wave's amplitude and phase are assumed to be slowly varying along the axis of propagation (z-axis), the left side of the wave equation can be written as:

$$\frac{\vec{\varepsilon}e^{i\alpha}}{k}\left[\vec{\nabla}_{\perp} + 2ik(\frac{\partial}{\partial z} + \frac{1}{c}\frac{\partial}{\partial t})\right]\mathrm{E} = -\frac{4\pi}{c}\vec{J}_{\perp}(\vec{x},t) \qquad (3.18)$$

and multiplying both sides by $k\hat{\varepsilon}e^{-i\alpha}$ to get

$$\left[\vec{\nabla}_{\perp} + 2ik(\frac{\partial}{\partial z} + \frac{1}{c}\frac{\partial}{\partial t})\right]\mathrm{E} = -\frac{4\pi}{c}\vec{J}_{\perp}(\vec{x},t)\bullet\hat{\varepsilon}e^{-i\alpha} \qquad (3.19)$$

this equation can be simplified further by introducing u = z-ct, which will follow the light as it travels. This is called "The Method of Characteristics", and the wave equation can now be written as:

$$\left[\vec{\nabla}_{\perp}{}^{2} + 2ik(\frac{1}{c}\frac{\partial}{\partial t})\right]\mathrm{E} = -\frac{4\pi}{c}\vec{J}_{\perp}(\vec{x},t)\bullet\hat{\varepsilon}^{*}e^{-i\alpha} \qquad (3.20)$$

where $\nabla_{\perp}^{2} = \partial_{x}^{2} + \partial_{y}^{2}$ is a measure of the diffraction of the optical field.

This is called the parabolic or paraxial wave equation with a source current $\vec{J}_{\perp}(\vec{x},t)$. The electron source current is the sum of all the single particle currents

$$\vec{J}_{\perp} = -ec\sum_{i}\vec{\beta}_{\perp}\delta^{(3)}(\vec{x} - \vec{r}_{i}(t)) \qquad (3.21)$$

Taking into account the transverse motion of the electrons (as it contributes to the transverse current density),

$$\vec{\beta}_{\perp} = -\frac{K}{\gamma}(\cos k_0 z, \sin k_0 z, 0) \tag{3.22}$$

If we substitute the transverse motion into the current density, and then substitute this new current density back into the wave equation in (3.19) and include $< e^{-i\zeta/\gamma} >$ which is the average over the sample electrons in the volume element we get

$$\left[\bar{\nabla}_{\perp}^{\,2} + 2ik(\frac{1}{c}\frac{\partial}{\partial t})\right] \mathrm{E} = -4\pi ieKk\rho(\vec{x},t) < e^{-i\zeta/\gamma} > \tag{3.23}$$

$\rho(\vec{x},t)$ represents the local electron density, $\zeta = (k + k_0)z - \omega t$ represents the electron phase. Each electron is uniquely indentified by its initial conditions.

To simplify the equation $|a| = \frac{4\pi NeKLE}{\gamma^2 mc^2}$ is re-introduced as the dimensionless laser field, the complex laser field is $a = |a| e^{i\phi}$, and the dimensionless FEL current is $j = 8\pi^2 Ne^2 K^2 L^2 \rho / \gamma_0^2 mc^2$. For simplicity, we can further assume that $\gamma = \gamma_0$ for all of the electrons during the interaction. The dimensionless transverse coordinates are defined as

$$\begin{aligned} \tilde{x} &= x\left(\frac{k}{2L}\right)^{1/2} \\ \tilde{y} &= y\left(\frac{k}{2L}\right)^{1/2} \end{aligned} \tag{3.24}$$

so that the equation will be completely dimensionless. The wave equation then becomes

$$\left[-\frac{i}{4}\bar{\nabla}_{\perp}^{\,2} + \frac{\partial}{\partial t}\right] a(\vec{x},\tau) = -\left\langle j e^{i\zeta} \right\rangle_{(\vec{x},\tau)} \tag{3.25}$$

All coordinates are now dimensionless for this form of the wave equation. Finally if diffraction is small and the electron/photon beam overlap is exact, the wave equation for the FEL can be written as

$$\overset{\circ}{a} = -j < e^{-i\zeta} > \tag{3.26}$$

The $j < e^{-i\zeta} >$ term on the right hand side of the equation is a measure of the bunching of the electrons. The evolution of the field a depends on the electron bunching. Likewise the evolution of ζ depends on the field a. This is a feedback loop and leads to the growth of the optical field. As ζ increases, so does the gain in the amount of bunching $< e^{-i\zeta} >$. This results in an exponential growth of the optical field until it reaches saturation. Saturation is achieved when the bunched electrons evolve further within phase space and begin to take energy from the optical beam vice give energy to it [1].

D. BEAM QUALITY

The last component of FEL theory that needs to be discussed is the importance of the electron beam quality. All of the preceding theory is based upon the assumption that the optical fields were transverse plane waves. Thus, for the equations to hold, or at least still be applicable, the electron beam needs to have limited divergence and be close to the center of the optical field. Thus, there are limits on the angular spread and overall beam radius of the electron beam. We quantify the overall beam quality by the transverse emittance of the electron beam via Equation 3.27.

$$\varepsilon = \sqrt{\langle x^2 \rangle \langle x'^2 \rangle - \langle x * x' \rangle^2} \simeq r_b \theta_b \tag{3.27}$$

For the purposes of this equation r_b = radius of the beam at the waist, and θ_b = the far-field beam divergence, x is the transverse position, and x′ is the transverse velocity. In addition to the transverse emittance we can define the normalized transverse emittance, which is conserved as the beam is accelerated.

$$\varepsilon_{normalized} \equiv r_b \theta_b \gamma \tag{3.28}$$

From $\dot{\nu} = {4\pi N \dot{\gamma}}/{\gamma}$ (3.14) we can see that changes in the Lorentz factor and phase velocity are proportional. A relativistic beam of electrons will have a finite spread of energy, resulting in a spread of phase velocities. This is another factor that determines the overall beam quality and is particularly important for the DFEA cathode work that is the focus of this thesis. The energy spread impacts the FEL interaction as well as the transportation of the beam as it is accelerated through our system.

THIS PAGE INTENTIONALLY LEFT BLANK

IV. FIELD EMISSION THEORY

This section will describe how we are able to get free electrons from a cathode by subjecting it to electric fields and the forces that these free electrons are subjected to as they travel between the cathode and anode.

A. POTENTIAL BARRIER AND QUANTUM TUNNELING

Any conducting material can experience field emission from its surface, provided a strong enough external electric field is applied. Traditionally, the only way for an electron to overcome the potential barrier, was to add energy to the electron until it exceeded the Fermi energy of the material. However, according to quantum theory, when an external field is applied to the surface of a metal, there is a reduction in the width of the potential barrier. As a result, electrons are able to tunnel through this reduced barrier and become free electrons. This phenomenon is a result of quantum mechanics, and was first studied by Fowler and Nordheim in 1928 [3].

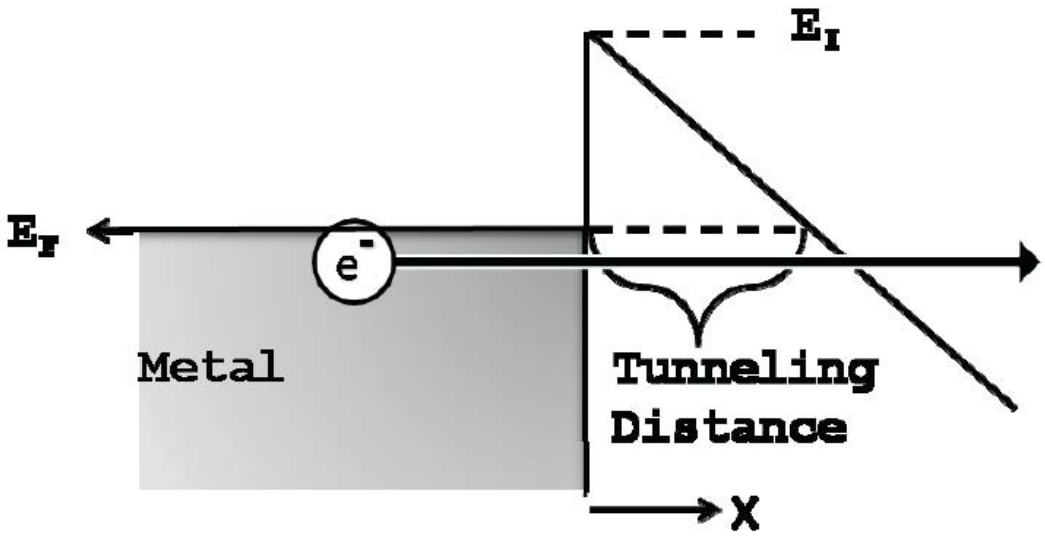

Figure 3. Depiction of Electron Tunneling through a potential barrier. The tunneling distance is reduced due to the applied electric field.(From [5])

In this case, the current density of the emission process is given by the Equation 4.1:

$$J = AE^2 e^{(-B/E)}$$
$$A = \frac{6.2x10^{-3}}{\Phi + \in_f}(\frac{\in_f}{\Phi})^{1/2}(A/V^2) \qquad (4.1)$$
$$B = 6.8x10^9 \Phi^{1.5}(V/m)$$

where E= the electric field at the material surface, Φ= the work function of the material, $\in_f$= the Fermi energy of the material. The constants A and B are related to the material's work function and Fermi energy [4].

B. FIELD ENHANCEMENT AND SURFACE PROTRUSIONS

Ideally, we could produce perfectly flat cathode surfaces; however, the reality is that no matter how finely we machine our surfaces; there are still small protrusions from the cathode. When electric fields are applied to the

cathode, the electric field lines converge at the tips of these protrusions and the result can be a significant enhancement of the electric field. The electric fields at these localized tips are represented as

$$E_m = fE \tag{4.2}$$

where E is the macroscopic gap field, and f is the field-enhancement factor. Initially, this phenomenon was viewed as undesirable; however, the diamond tipped field emitter arrays that will be tested embrace this effect. For a perfect micro-protrusion, the field enhancement factor can be determined by

$$f = \frac{(\lambda^2 - 1)^{1.5}}{\lambda \ln[\lambda^2 + ((\lambda^2 - 1)^{0.5}] - (\lambda^2 - 1)^{0.5}}, \tag{4.3}$$

where λ = h/b, h is the protrusion height above the cathode plane, and b is ½ the width of the protrusion's base [4].

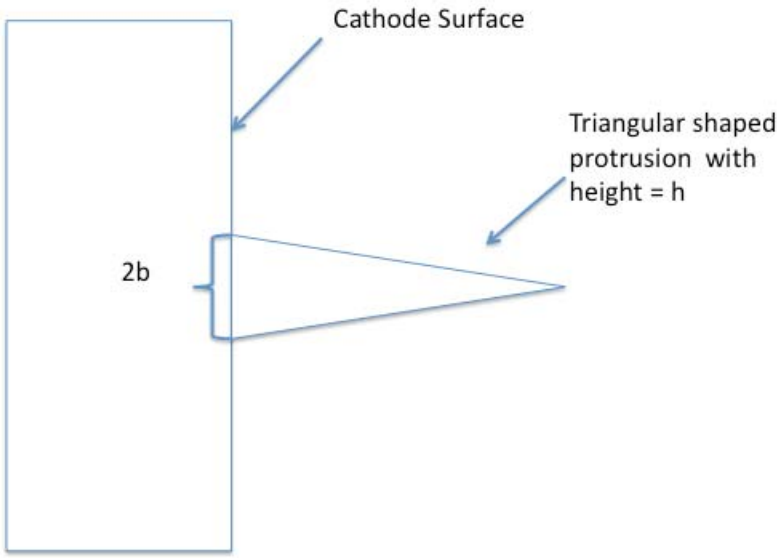

Figure 4. Diagram of a protrusion (triangular in shape) from the surface of a cathode. The protrusion is of height h, with a base of 2b.

In early experiments, this effect occurred for only a brief time before the protrusions evaporated due to Joule heating, which results from high localized currents caused by the high electric field localization. In order to take advantage of this effect, a more durable material was needed. Diamond was the perfect choice, due to its durability and high thermal conductivity. Even under high electric fields and large emission currents, the diamond "pyramids" were able to function as designed for prolonged periods of time.

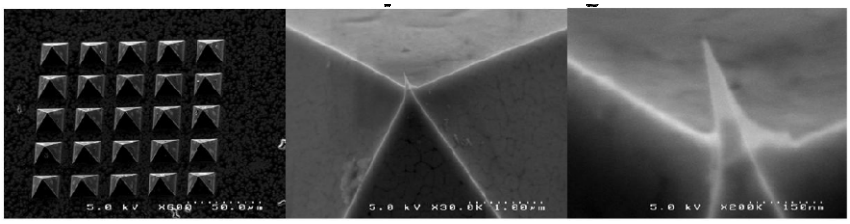

Figure 5. Images of the Vanderbilt University DFEA cathode surface. Individual tips are on the order of microns in size.(From [6])

C. ELECTRIC FIELDS AND ELECTRON TRAVEL

Another essential component of a field emitter array is the shape of the electric field lines and equipotential lines at the surface of the array. The goal is to have a uniform electric field gradient normal to the cathode (except at the cathode tips). This will ensure that all of the tips of the field emitter will experience the same electric field, and thus all emit uniformly. To achieve this, we are implementing a Pierce-like geometry. This geometry entails angling the edges of the cathode surface in the direction of electron travel. Figure 6 gives a representation of the initial Pierce-like geometry that we are employing for the cathode-anode ring.

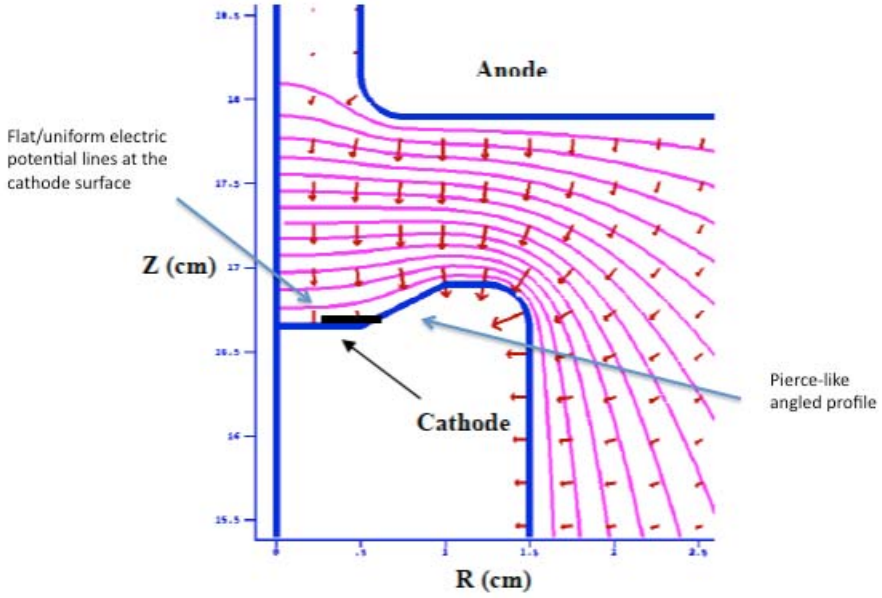

Figure 6. Example of the initial pierce-like geometry that was the starting point for the cathode design. Note that this is a side view of half the cathode/anode configuration (From [7])

When the electrons are emitted, they are subjected to a force due to the electric field ($F = eE$). This force acts perpendicular to the electric potential, thus the electrons will travel perpendicular to the potential lines. The electric field lines will only affect the electrons while they are traveling between the cathode and the anode (once through the anode gap the fields quickly diminish in strength). When the electrons are past the anode gap, they will essentially be free from the initial acceleration forces.

In addition to the force that the electrons will experience due to the electric field, they will also be subjected to "space charge" forces from neighboring electrons. Once emitted, the electrons form a cloud of charged particles. Since each electron is negatively charged, electrons will tend to repel each other. This small effect between individual electrons, can lead to a large diffusion of the overall electron beam that is emitted from the cathode. The geometry of our cathode-anode configuration helps to minimize this effect by having a fairly flat equipotential between the cathode and anode. Additionally, at low currents, these forces are not as strong as the force due to the applied electric field, and the electron beam should remain approximately co-laminar, at least for our configuration. A high-current FEL injector beam will experience significant space charge forces, and must be designed to compensate for them, but that is beyond the scope of this thesis.

THIS PAGE INTENTIONALLY LEFT BLANK

V. FIELD EMITTER ARRAY CATHODE TEST CELL DESIGN

In normal practice, injectors are designed to use one specific type of cathode and the rest of the FEL system will adjust to the beam that is produced. This can be limiting to research, since changing or replacing damaged cathodes can be expensive and time consuming. Instead of testing new cathode configurations directly with the entire FEL system, cathode test cells are used. These test cells provide a convenient apparatus to study various cathodes and the electron beam that is produced, and they allow for easy modifications. This thesis will only deal with the specific DFEA cathodes supplied to the Naval Postgraduate School by Vanderbilt University. The test stand that Vanderbilt used to study the effects of these cathodes, is shown in Figure 7. This test stand is used for low voltages (approximately 1KV) with a 1mm gap between the cathode and anode. Additionally, Vanderbilt employed the use of a gridded anode (which we will not be using) [8].

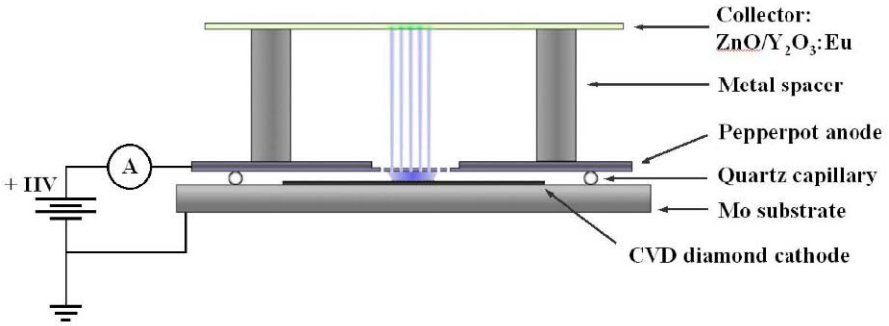

Figure 7. Vanderbilt University DFEA Cathode Test Cell (From [9])

Although we are going to be using the same type of diamond tipped field emitter array as Vanderbilt, our cathode test cell is designed to study the effects of using these DFEAs in conjunction with a high voltage and a un-gridded anode. This will provide insight into the potential uses for DFEA in higher energy systems. Additionally, by having higher electric fields, the electrons that are produced will be subjected to a greater force and be closer to the relativistic speeds at which the rest of our FEL system operates. Thus, this is a step towards the use of these types of cathodes with FEL injectors.

A. CATHODE-ANODE DESIGN REQUIREMENTS AND GEOMETRY SELECTED

The DFEA requires an electric field of 10-20 MV/m in order to "turn on" and thus start producing electrons [8]. This is the first and most crucial design requirement that needs to be met for the cathode geometry. In addition, the electric field lines need to be uniform along the surface of the DFEA. This will ensure that all of the individual emitter tips will experience the same field and hopefully emit uniformly. The cathode will be at minus 100KV and the anode will be at ground. With these parameters in place we were able to vary the shape of both the cathode and anode and the distance between them.

The starting point for the construction of the cathode involved using a Pierce-like geometry; including angling the outer edges of the cathode in the direction of the electron travel with a flat section in the center. This geometry helps to flatten the electric fields along the

inner surface of the cathode where the DFEA shall be placed. The initial shape of the anode was chosen to see if there was any appreciable change to the field and the surface of the cathode with a long thin inner lip portion. This shape did little to change the fields at the cathode surface and was thus abandoned in favor of easier to machine geometries. One problem with this initial design is field enhancement at the outer edges of the cathode due to this shape. Initially, the edges of this sloping portion of the cathode (Figure 8) were not rounded.

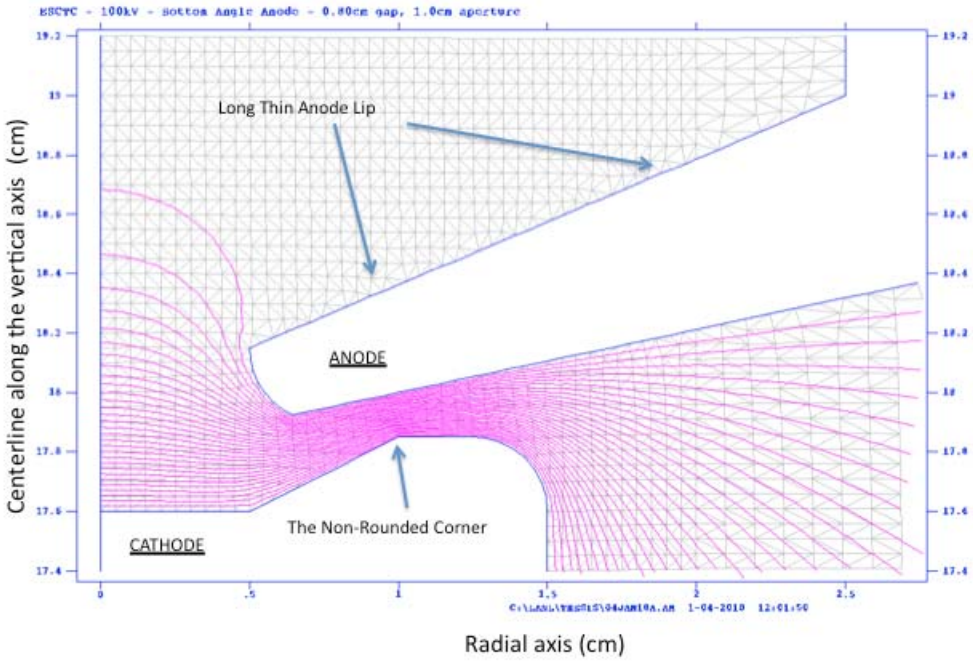

Figure 8. Side-view of the initial cathode and anode geometry created in Poisson Superfish (From[10])

The desired field along the inner surface of the cathode was attained, but a potential problem could arise from this design. This design has a corner at a location

where the electric fields were enhanced, and with such high electric fields the possibility of field emission from these corners and the generation of a plasma arc was a valid concern. As such the geometries were smoothed out and another preliminary design was generated. All of our field requirements were met and we simulated the effects of having a very small lip on the inner surface of the anode. This change in the shape of the anode was done to see if having a slightly recessed geometry would be worth the additional machining time and effort.

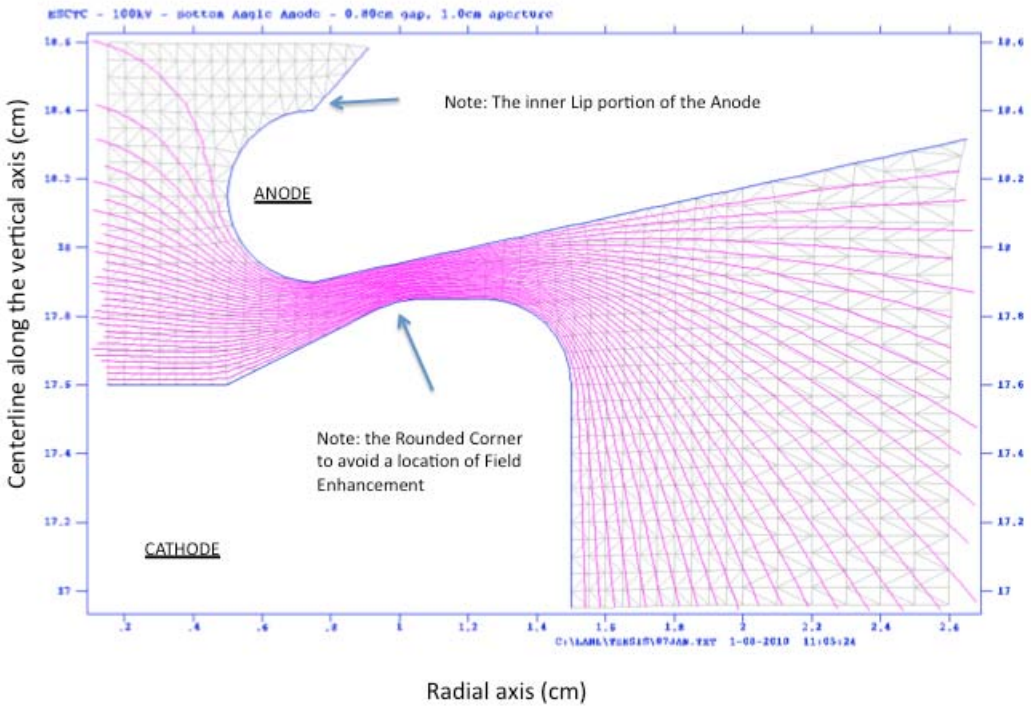

Figure 9. Second cathode and anode design geometry. Note the rounded edges.

Although there were some very slight changes to the electric potential lines between the cathode and anode, due to having this small inner lip, they were quite insignificant, and the additional complexity that would be added to machine this anode geometry, was deemed to be not worth the effort. Therefore, some additional adjustments were made and the final cathode-anode geometry was produced and is seen in Figure 10.

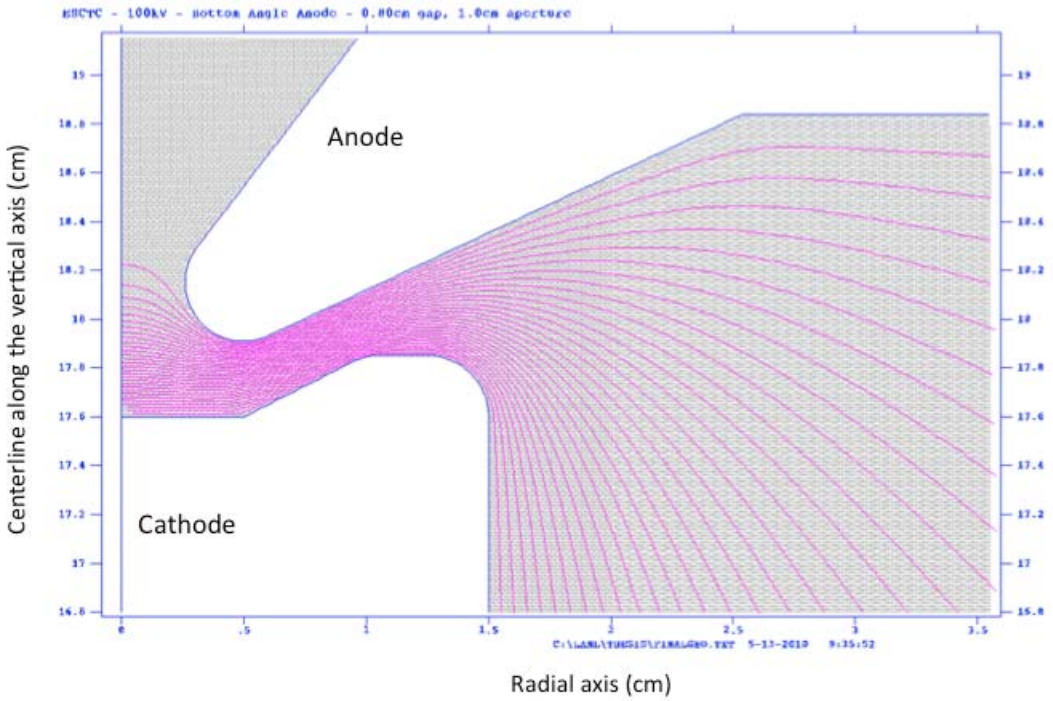

Figure 10. Final Design Geometry for the Cathode and Anode configuration for use in the Cathode Test Cell.

Note that the electric potential lines in Figure 11 along the inner portion of the cathode are not completely uniform; however, the variance is approximately 2% over this section and at the lowest point it is well above the minimum field needed to activate the DFEA.

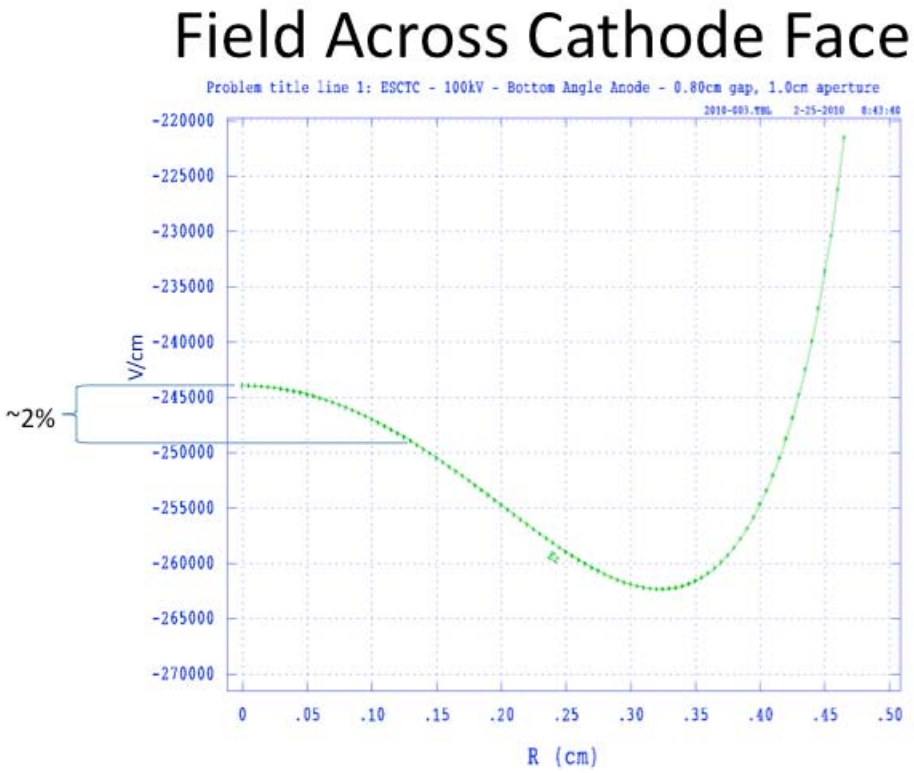

Figure 11. Electric potential across the inner flat surface of the cathode face.

Since we will be able to control the gap distance between the cathode and anode, this small variance will allow us to locate the ideal spacing where the DFEA tips are "Turned On."

A 3-dimensional schematic of our final Geometry was created using the SolidWorks [11] computer-aided-design program. Here the 2-dimensional model that was used to simulate the electric fields within Poisson-Superfish was transferred into SolidWorks. Since the cathode and the anode are two separate components, each one had to be modeled separately. These 3-dimensional models are the blueprints from which the actual components were

fabricated. SolidWorks is able to create both a visual and a detailed framework of the parts that can then be exported electronically for fabrication. The final cathode and anode designs are shown in Figure 12. For a visual aid, the DFEA is included to shows its approximate location within the cathode. Also, there are drilled holes in the anode, and a screw hole in the cathode that were designed as mounting points to the rest of the test cell.

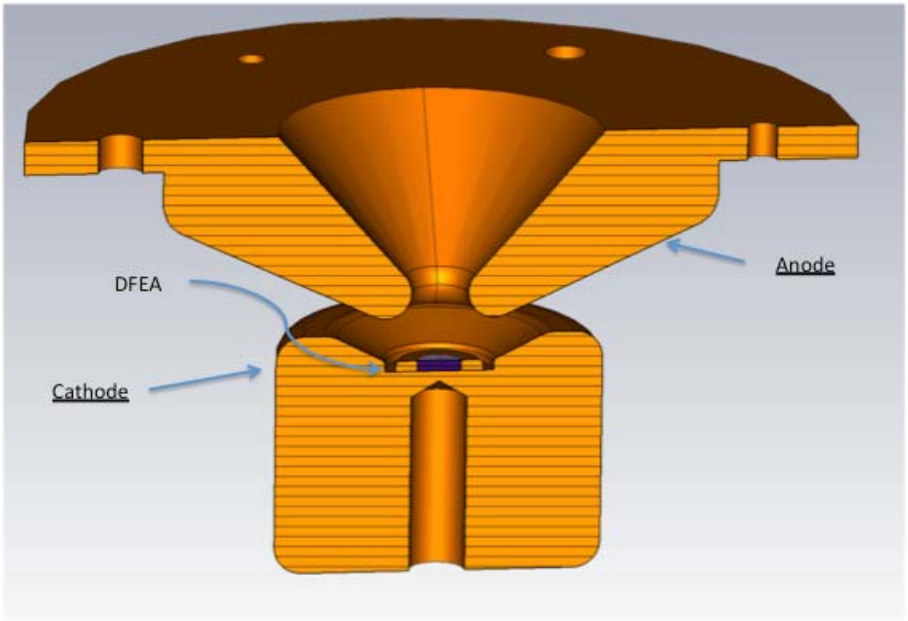

Figure 12. Composite image of the cathode and anode geometries created from the Poisson-Superfish design

B. TEST CELL DESCRIPTION, DESIGN, AND CONFIGURATION

The test cell is comprised of the additional components that will house the cathode and anode at vacuum and allow for the experiment to be conducted safely.

Figure 13 represents the basic layout that was used as the starting point for the SolidWorks design configuration.

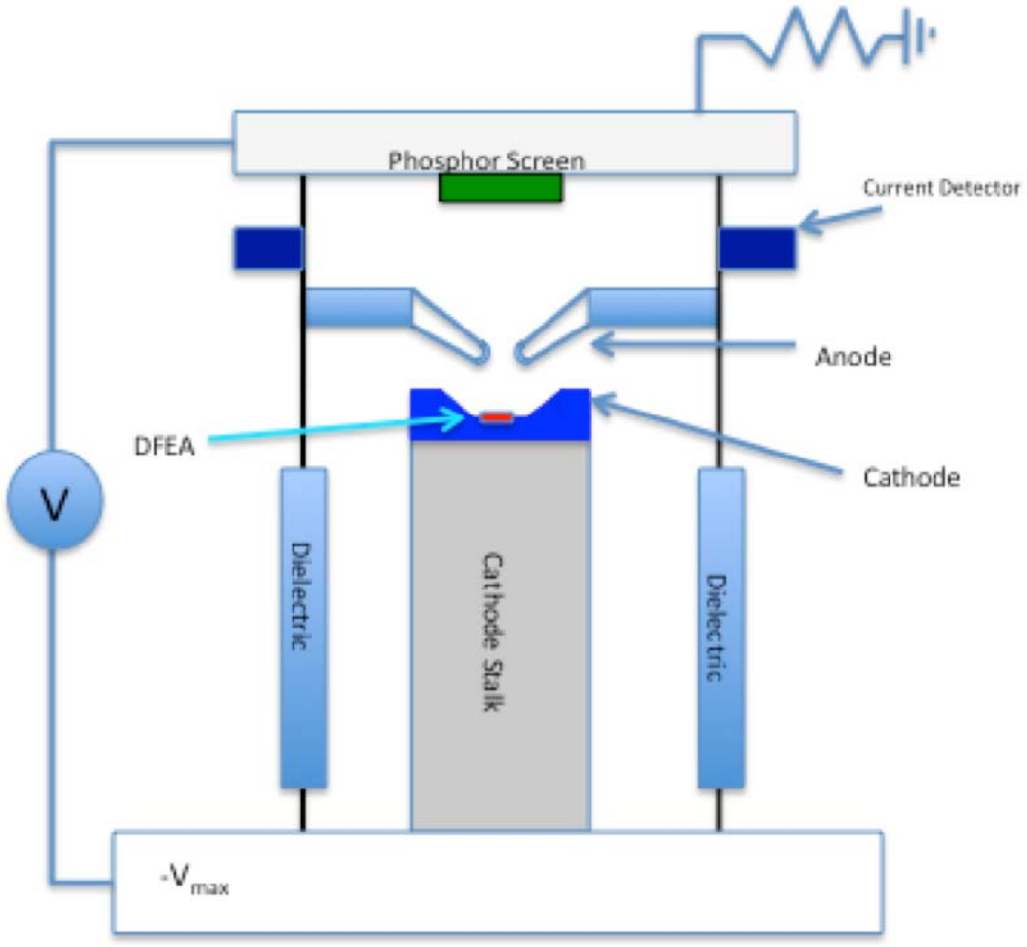

Figure 13. Diagram of the Cathode Test Cell configuration.

Because this experiment will be carried out using a high-voltage power supply, it is important that the test cell that is used be safe, easy to access, and easy to modify. When the experiment is carried out, it will be done at vacuum, and there will be a phosphor screen mounted above the anode in order to image beamlets that are emitted from the DFEA. It is important to note, that although the substrate on which the DFEA is supplied to us will be

circular (approximately 8mm in diameter), the individual array points will have a cross-shaped pattern vice filling the entire circular shape of the DFEA substrate. Figure 14 illustrates this point.

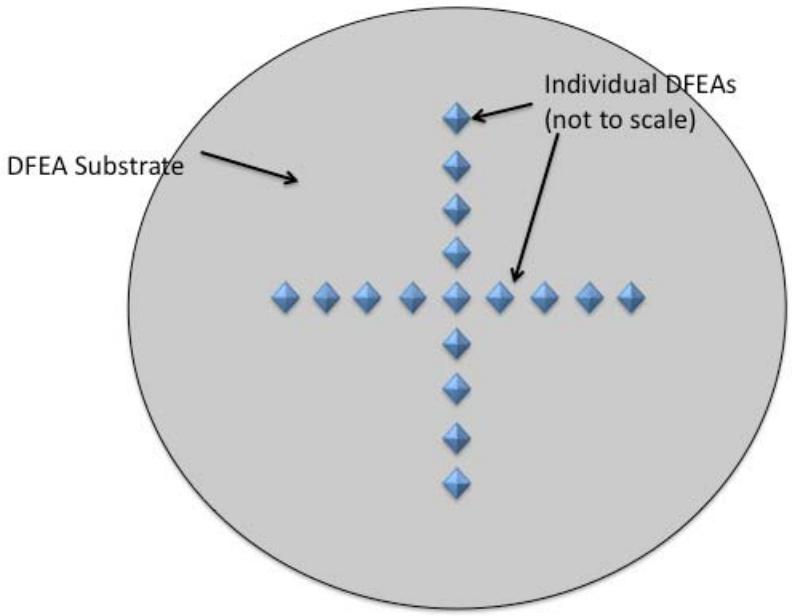

Figure 14. DFEA on a substrate showing the location of the individual emitter tips.

This shape allows for imaging of the individual beamlets to study how the DFEA is being activated within our system, while keeping the number of tips, and generated current, to a manageable number. This will provide feedback as to the positioning of the anode relative to the cathode and help to make adjustments as necessary.

To control the gap spacing between the cathode and the anode (as well as the relative alignment between these two components), the anode is mounted on a plate that is resting on three mounting rods, which are connected to three servomotors. Also, connected above the anode, will be the phosphor screen, as seen in Figure 15.

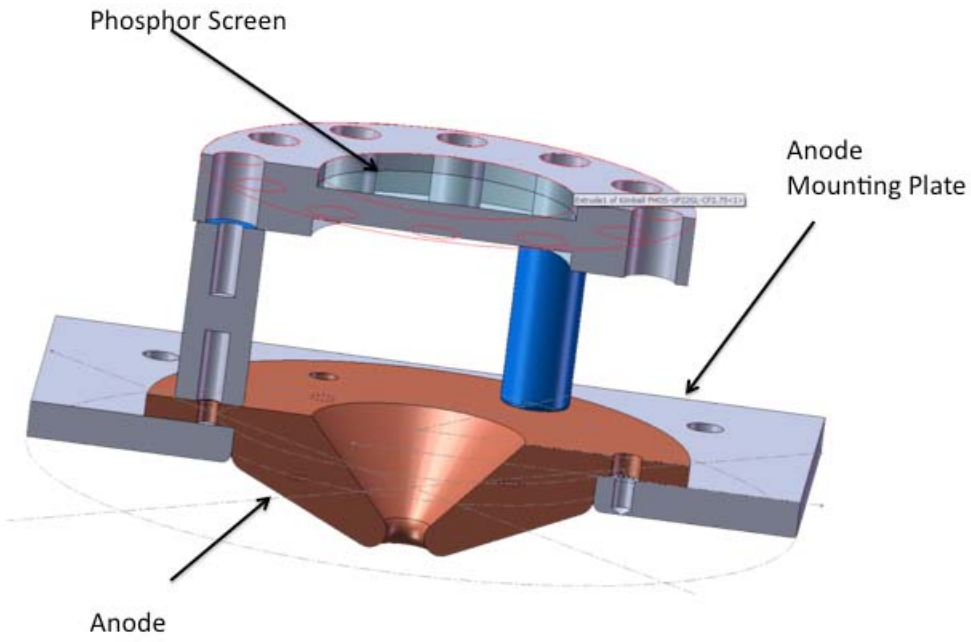

Figure 15. Composite of the anode and the phosphor screen, which will be used to image the electrons from the DFEA.

Figure 16 shows the anode configuration with the attached motors.

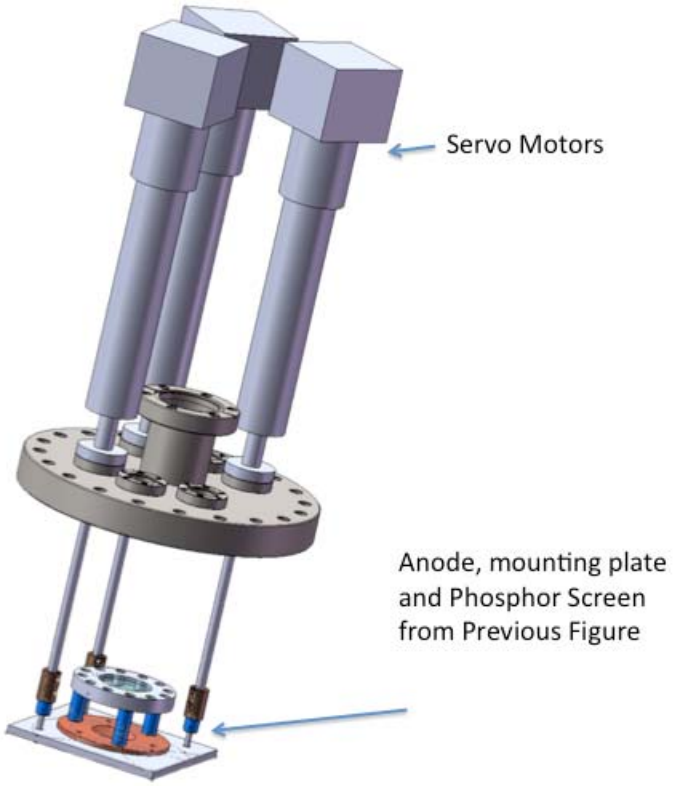

Figure 16. Solidworks composite of the upper cathode test cell assembly.

This assembly along with the cathode will be housed within a 6-way cross with 8" ports for easy access and diagnostic mounting. One of the fantastic features of SolidWorks is its ability to link with commercial suppliers. This allows for the test stand to be designed with COTS products (which can be seen in Figures 15 and 16).

The total enclosed cathode-anode test assembly is seen in Figure 17.

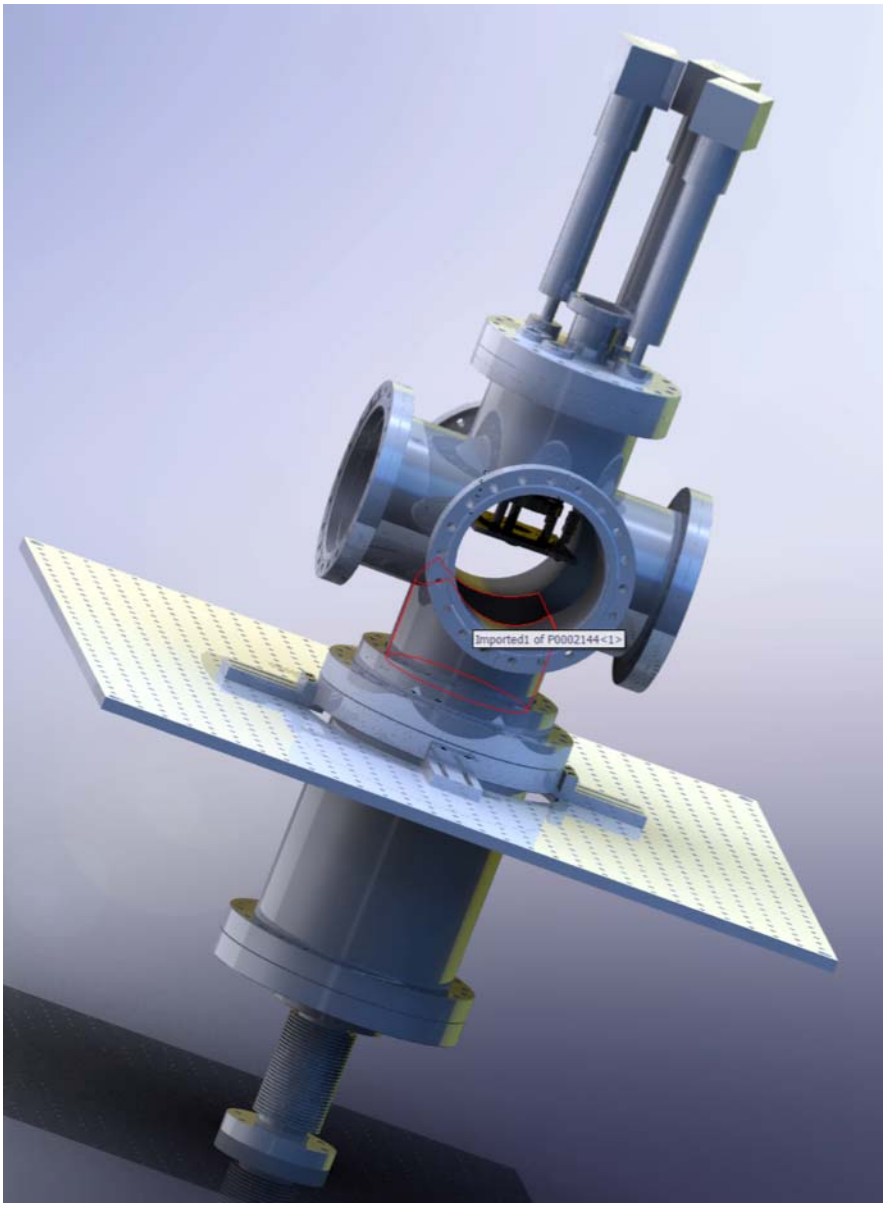

Figure 17. "Smoke Stack" enclosed cathode test cell assembly mounted to the optical table.

The last piece of the puzzle needed to complete our test stand was the physical stand that the cathode-anode test assembly will sit upon. Using a 30" by 30" optical table as the stand top, a 10" hole is cut and the assembly will be mounted at this location. The optical table will then sit upon a wheeled aluminum frame (Figure 18). This

is the completed representation of our test-stand. However, it should be noted that there are no open accesses within the test frame. There is a wire-mesh screen that is inserted to prevent accidental access to the high voltage portion of the system. This is done as a safety precaution. The only access to the interior of the test-stand frame will be through a latched access door. Additionally, there is an interlock that will not allow the system to be energized unless the door is secured. This, of course, is a required safety precaution.

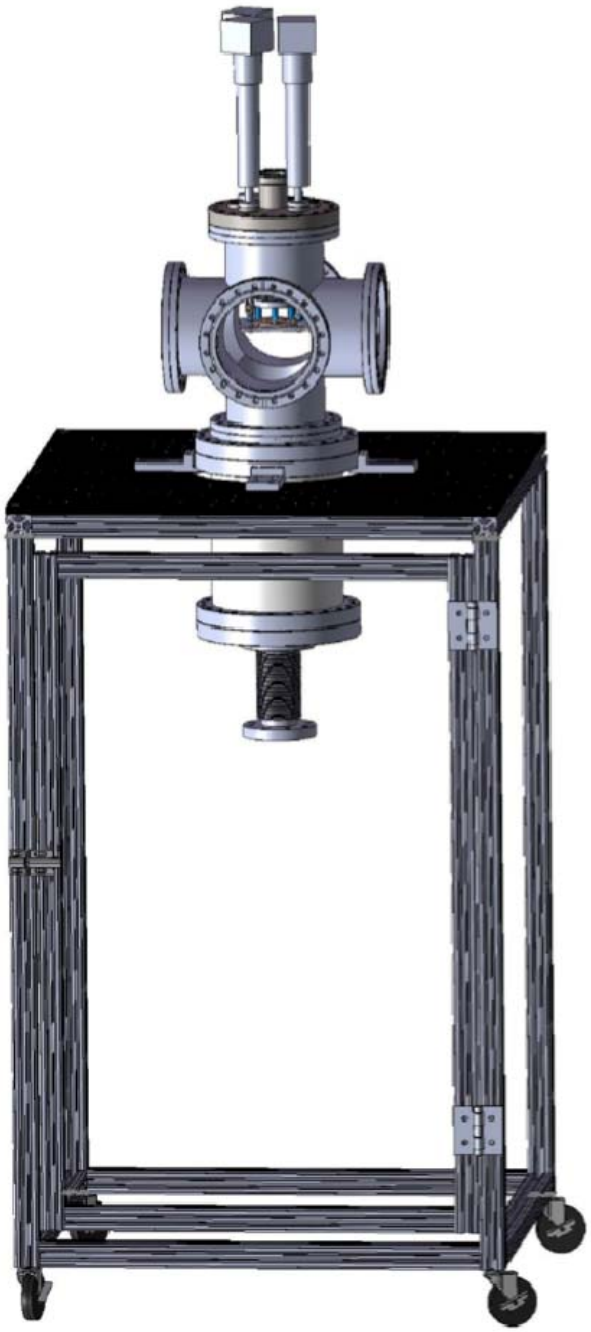

Figure 18. Complete cathode test cell assembly rest on the movable test stand. This will be the configuration used for experimentation. Note that the door will be interlocked and there are mesh screens in the test stand side panels.

VI. FIELD EMITTER ARRAY SIMULATION

With the design of the test cell complete the next step is to create a simulation of how the cathode will function when energized. The goal of this simulation is to create a working model that will give us additional insight into an optimal choice for the cathode to anode gap spacing.

When the geometries for the anode and cathode were created a gap size was chosen (0.80 cm) that ensured the electric field requirements for the DFEA were met. However, this is not the only spacing that can meet the electric field requirements. In fact the initial design essentially helped to establish an operating range for the spacing of the cathode to the anode. The simulations that will now be discussed follow the electrons as they leave the surface of the cathode and travel through a gap driven by an RF field, as they would in an FEL injector.

These simulations will track the phase, time out of the gap, and normalized momentum of the electrons as they travel through the gap. From there we will see how the average energy of the electrons and the energy spread vary as a function of the gap spacing. The results from this "Beam Code" (see Appendix, section A) will then be used as the input for Spiffe [12], which is an accelerator gun code that can model cathode cavities. The output from Spiffe will be a reasonable approximation of what we can expect from the output of our cathode test cell. Thus, this will provide an initial comparison point from which to conduct experimentation.

A. DETERMINING THE INITIAL BEAM CHARACTERISTICS

The simulation program was created using input parameters (gap spacing, electric field, and phase angle of emission). Initially, the electric field is treated as uniform over the gap spacing

$$E = \left[E_o \cdot \sin(2\pi \cdot f \cdot t + \phi)\right] \tag{6.1}$$

The output of this program provides us with the input parameters necessary for the Spiffe code. This "Beam Code" was created in three major stages. The first is to create a graph of the $\beta\gamma$ (normalized momentum) versus the phase at which the field emitter will produce electrons for a given gap spacing. The second stage modifies this program to run over a range of gap spacings. The final iteration is to use a non-uniform electric field similar to that which will be used in our quarter wave injector here at NPS. The formulas, relations, and definitions that were used to create the "Beam Code" program are specifically applicable to particle accelerator applications. They were provided by Dr. John Lewellen (personal communication, January 4, 2010) and summarized in the Appendix, section B.

For this simulation the magnetic field was assumed to be zero, which greatly simplifies the equations. The "Beam Code" computer simulation integrates the change in position with respect to time and couples that with the change in the normalized momentum with respect to time. Picoseconds were chosen as the time step and the program integrates over approximately a nanosecond. Additionally, the program exits the integration should the electron go beyond the region of interest for us (which is from z=0 to z=L=the gap

spacing, see Appendix, section A). Outside of this region the electric field is zero and the particle is no longer under the influence of our cathode geometry.

The initial program iterations proved to be very successful and the desired $\beta\gamma$ vs. phase profile was achieved. Note that a gap spacing of 0.80 cm is used for this stage of the program, as this was the previously designed gap spacing. It also important to note that this program tracks a single electron as it travels through the gap.

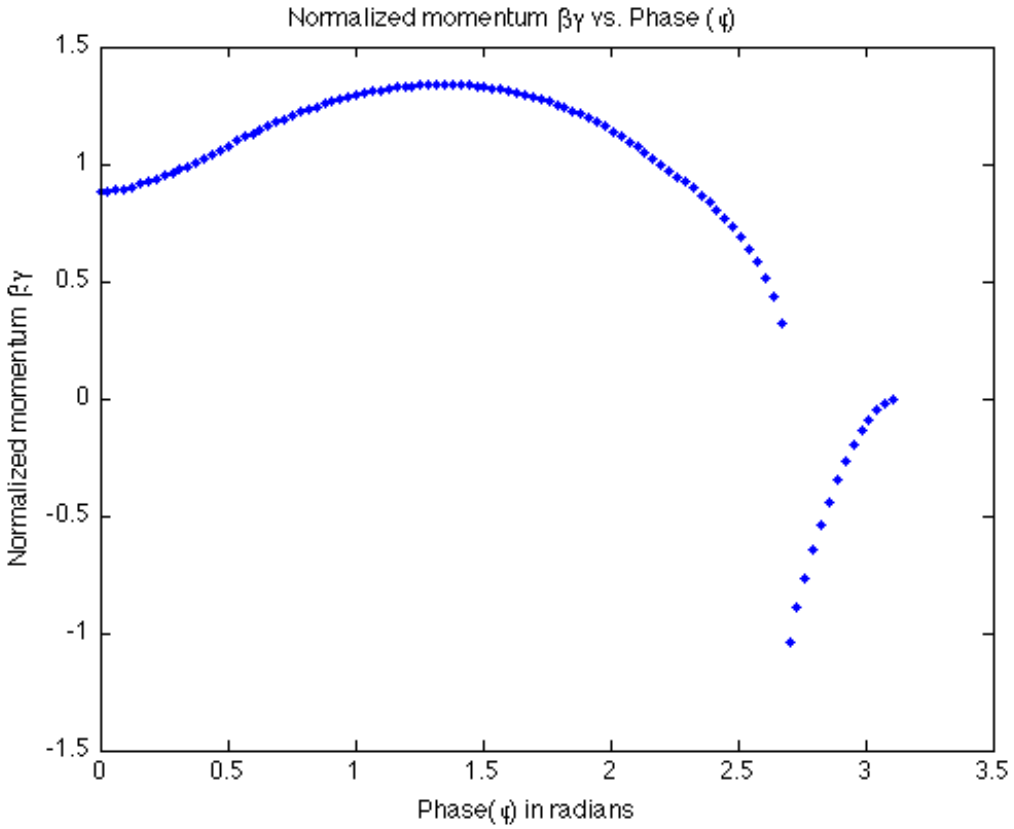

Figure 19. Normalized momentum ($\beta\gamma$) vs. emission phase for a 0.80 cm gap. Note that the electron emission is assumed at each phase, whether or not an electron would actually be emitted due to the applied electric field.

In addition a graph of $\beta\gamma$ as a function of tout (time at which an electron exists cavity) was created. This provides a feel for the output momentum of the electrons as a function of the time to reach the aperture within the anode (t-out).

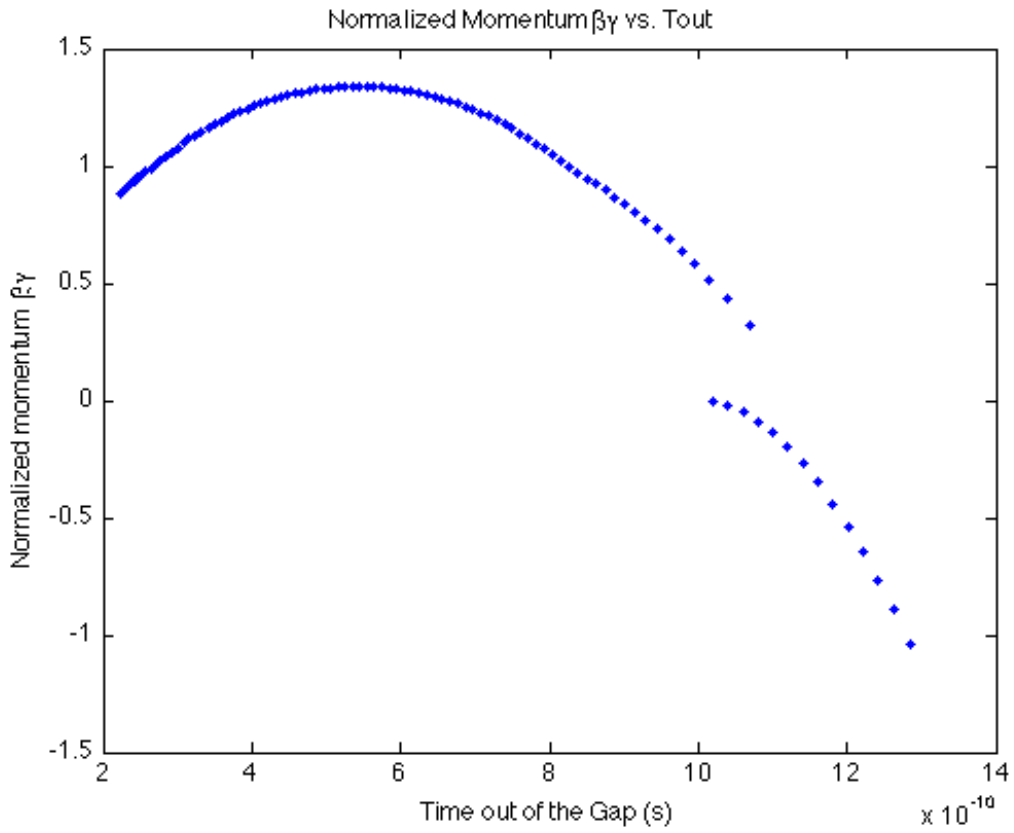

Figure 20. Normalized momentum ($\beta\gamma$) vs. the time it takes the electron to transit through the gap spacing. A gap spacing of 0.80cm was used for this graph.

Likewise, a graph of the t-out as a function of the phase was constructed.

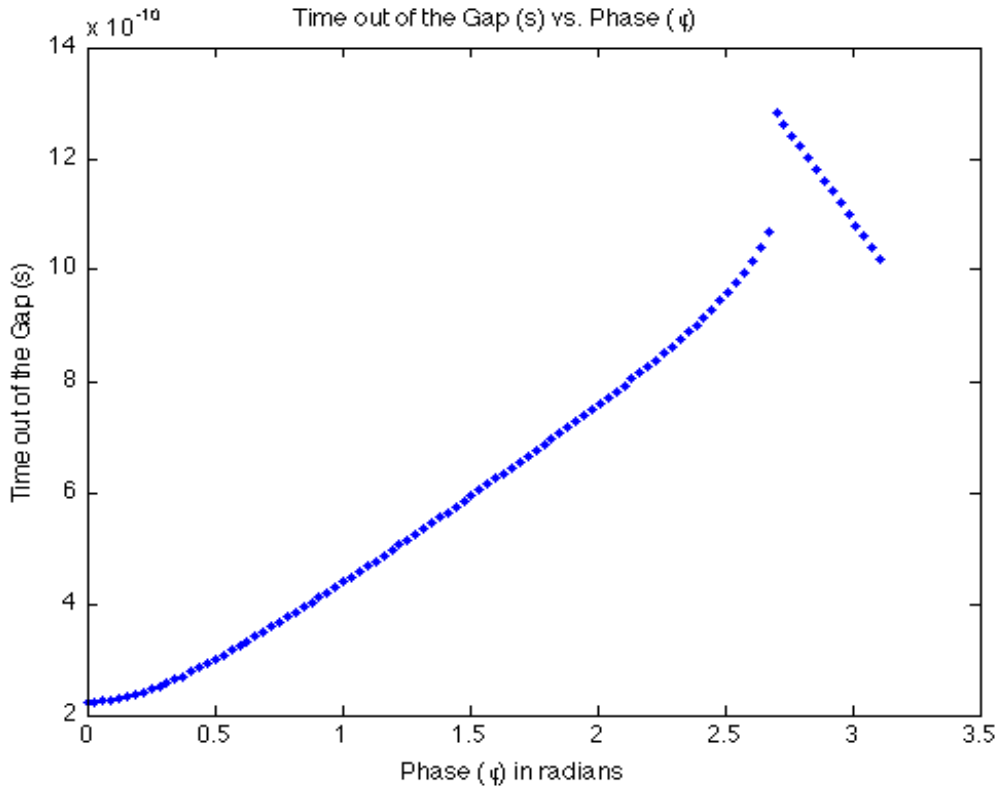

Figure 21. Time it takes an electron to transit the gap between the cathode-anode and the phase of the electron.

Looking at Figures 19, 20, and 21, we can see that the electron will have the greatest normalized momentum ($\beta\gamma$) at an emission phase of approximately 1.35 radians, at roughly 500 picoseconds transit time (with at 0.80cm gap spacing).

Next, we modeled the current density of the beam as a function of phase (ϕ). Based on the results from [13], a Gaussian distribution was chosen to model the current density (J). A sigma of 10^{o} was determined as a reasonable estimate for the width of the current pulse in this Gaussian model [13]. The equation for the current density is given as

$$J = A \cdot e^{-\left[\frac{\left(\phi - 90^\circ \cdot \frac{\pi}{180^\circ}\right)}{\left(2 \cdot 10^\circ \cdot \frac{\pi}{180^\circ}\right)}\right]^2} \qquad (6.2)$$

Since we are only interested in where J is maximized, the value for the amplitude of the current is arbitrary (A set to 1 for the simulation). The following graph is of normalized current density (J) as a function of the phase angle (ϕ) for electron emission.

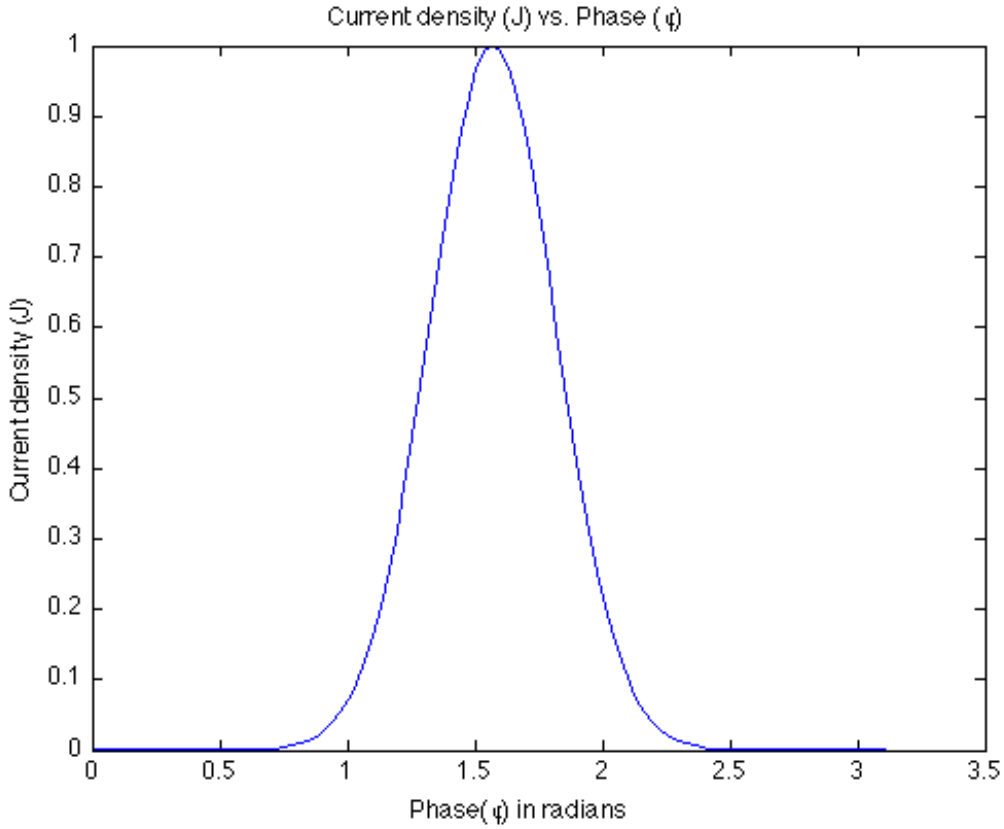

Figure 22. Current density vs. phase of electron emission for a 0.80cm gap.

Here the peak current density occurs at ϕ=1.5708 radians. This is not the same peak as the normalized momentum vs. phase graph. The normalized momentum, phase,

and current density, are coupled to construct a beam profile graph. In this graph, J is used to weight the value of the normalized momentum.

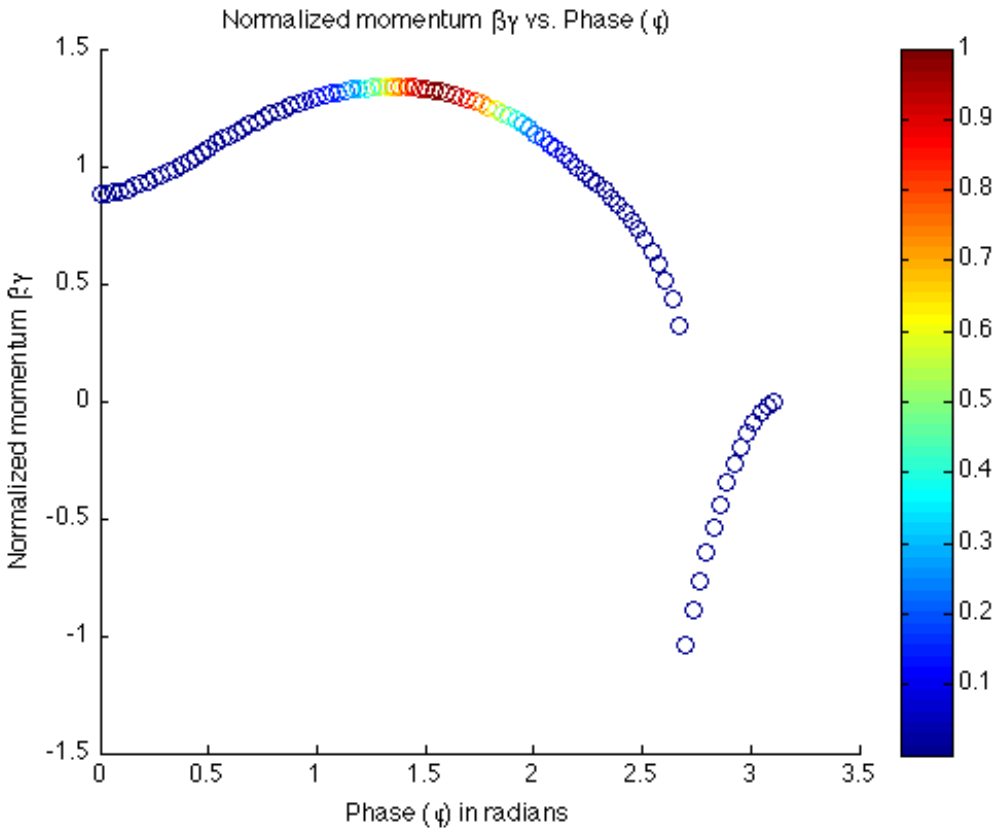

Figure 23. Normalized Momentum ($\beta\gamma$) vs. phase weighted by current density (J)

Additionally, a graph of the normalized momentum, as a function of T-out weighted by the current density, was created.

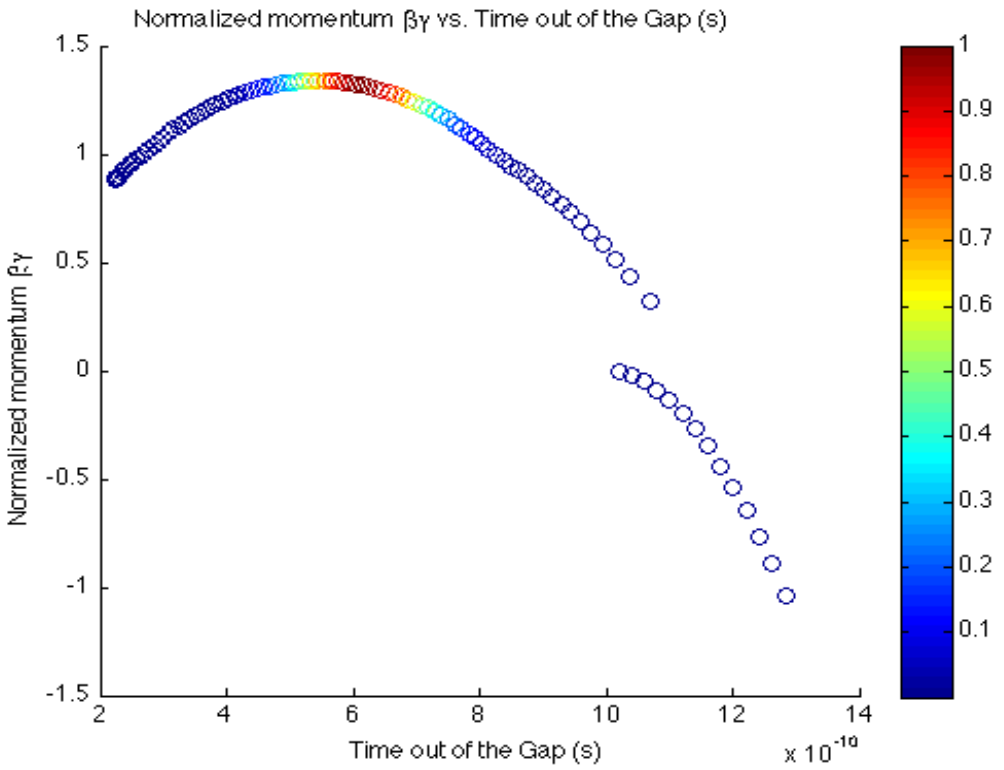

Figure 24. Normalized Momentum ($\beta\gamma$) vs. time it takes the electron to leave the gap (tout) weighted by current density J.

Figures 23 and 24 show that the current density occurs over a relatively compact section of the normalized momentum, with regard to both phase and time, which indicates that energy spread for this beam is not very large. A small energy spread is beneficial to our system; however, this is only for single gap spacing of 0.80cm. Thus, the program is now modified to track the average beam energy and energy spread as a function of gap distance (L), phase (ϕ), and time (t). In order to do this both the average energy <E> and the energy spread σ_E are calculated quantitatively

$$< E >= \frac{\sum \beta\gamma(\phi) \cdot J(\phi)}{\sum J(\phi)}$$

$$\sigma_E = \sqrt{\frac{1}{N}\sum(\beta\gamma(\phi) - < E >)^2} \qquad (6.3)$$

(N = the number of particles)

Figure 25 shows the average energy as a function of the gap spacing. It increases in a non-linear fashion as the gap spacing increases; which is expected.

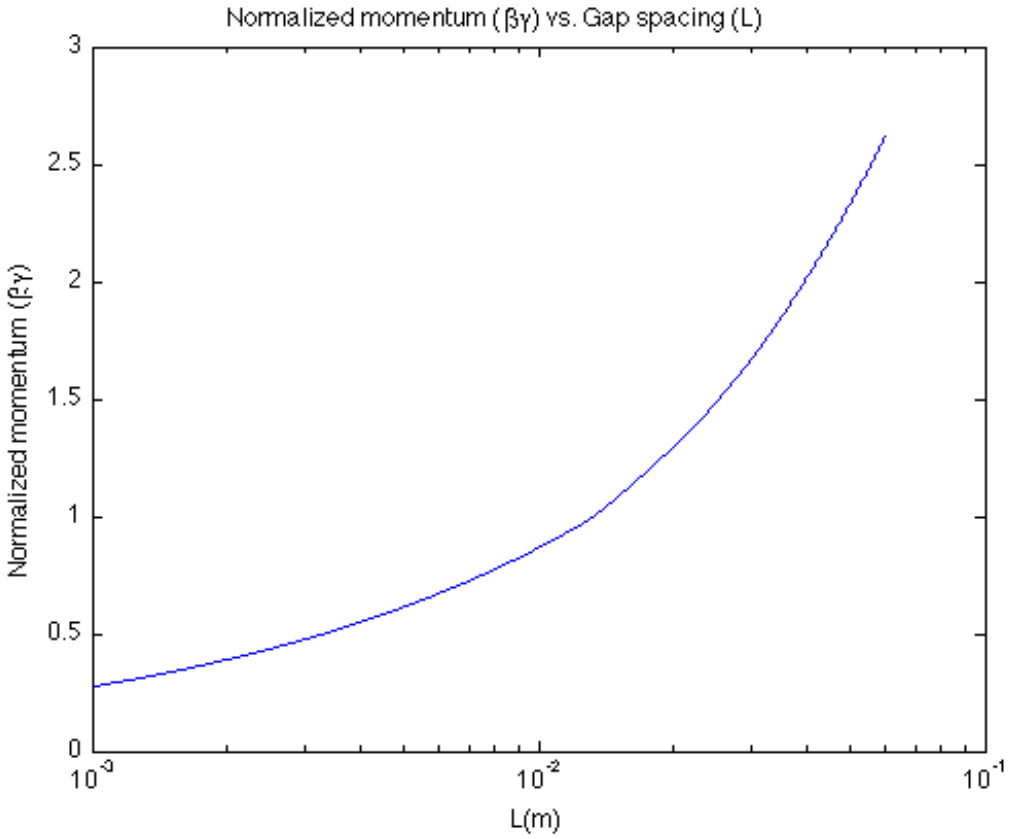

Figure 25. Average energy vs. the gap spacing between the cathode and anode

Figure 26 shows the energy spread as a function of gap spacing. At very small gaps, the energy spread is quite high, and then drops down quickly to a minimum value at

1.28cm with a value of 0.02686. From Figure 26, it can be seen that when the gap spacing is larger than 3mm, the overall energy spread is not that great. The ideal point to operate would be with a gap of 1.28cm; however, using our previously design gap value of 0.80cm, the energy spread is only 0.0277, which is still a good location for operation.

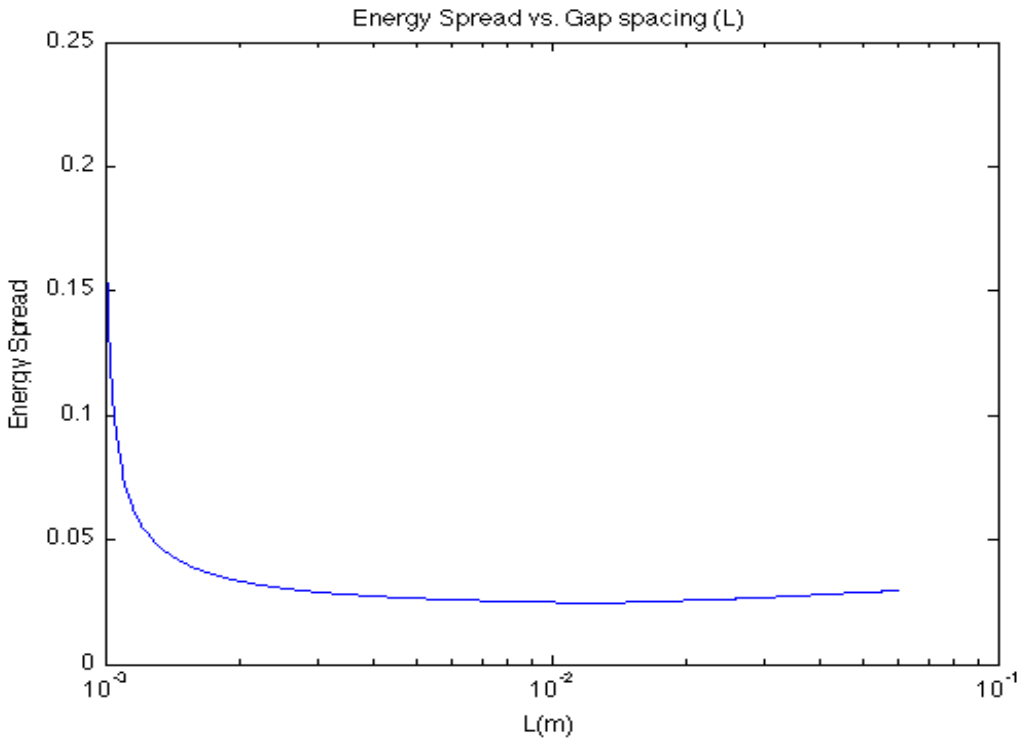

Figure 26. Energy Spread vs. gap spacing between the cathode and anode

All of the simulations so far have used an electric field modeled to be uniform along the axis of electron travel (z axis for these simulations); however, with the quarter wave RF gun that NPS will be utilizing, the electric field changes as the distance varies. The electric field within the quarter wave gun can be approximated as follows

$$E = \left[E_o \cdot \sin(2\pi \cdot f \cdot t + \phi)\right] * \left(1 - \frac{z}{L_{gap}}\right) \qquad (6.4)$$

Figure 27 illustrates how this non-uniform electric field affects the energy spread. Overall the energy spread is reduced but the minimum value shifts to L = 2.56 cm, much larger then our designed test cell gap of 0.80cm. However, the energy spread at 0.80 cm is still quite small. Therefore, using a gap spacing of 0.80cm is still acceptable.

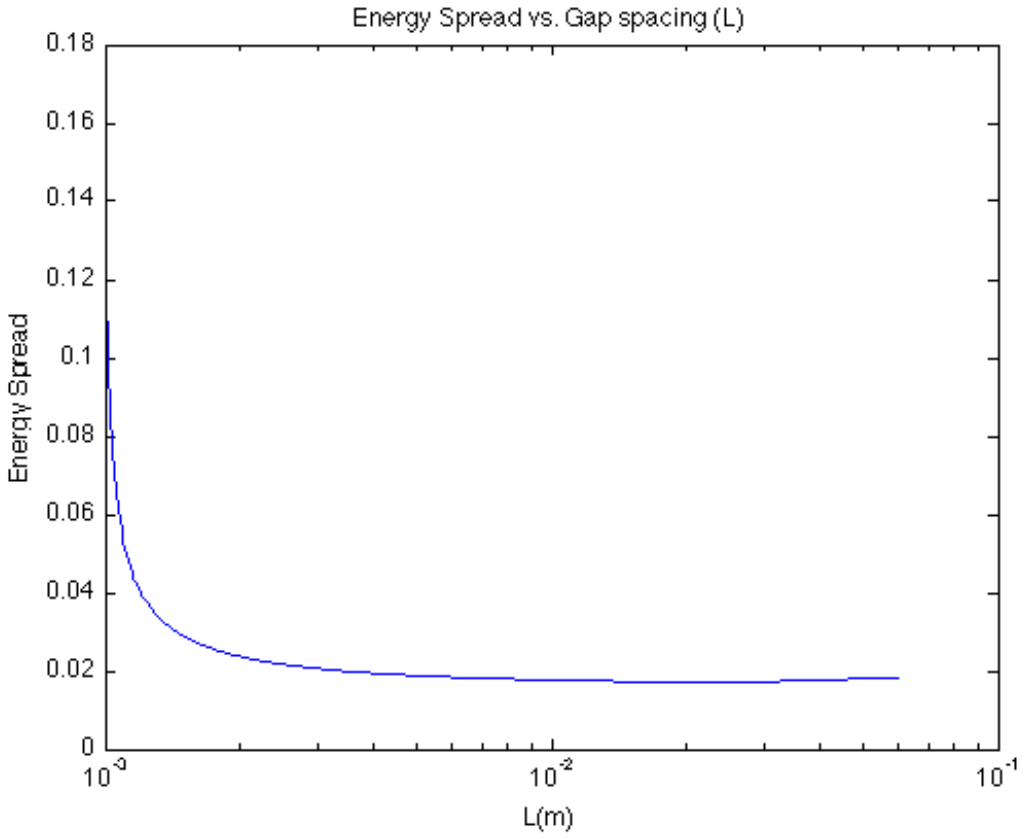

Figure 27. Energy Spread vs. gap spacing between the cathode and anode with a non-uniform electric field

The average energy of the electron beam is decreased as a result of the non-uniform electric field, and is seen in Figure 28. Note that the overall shape has not changed from the case where the Electric field was uniform.

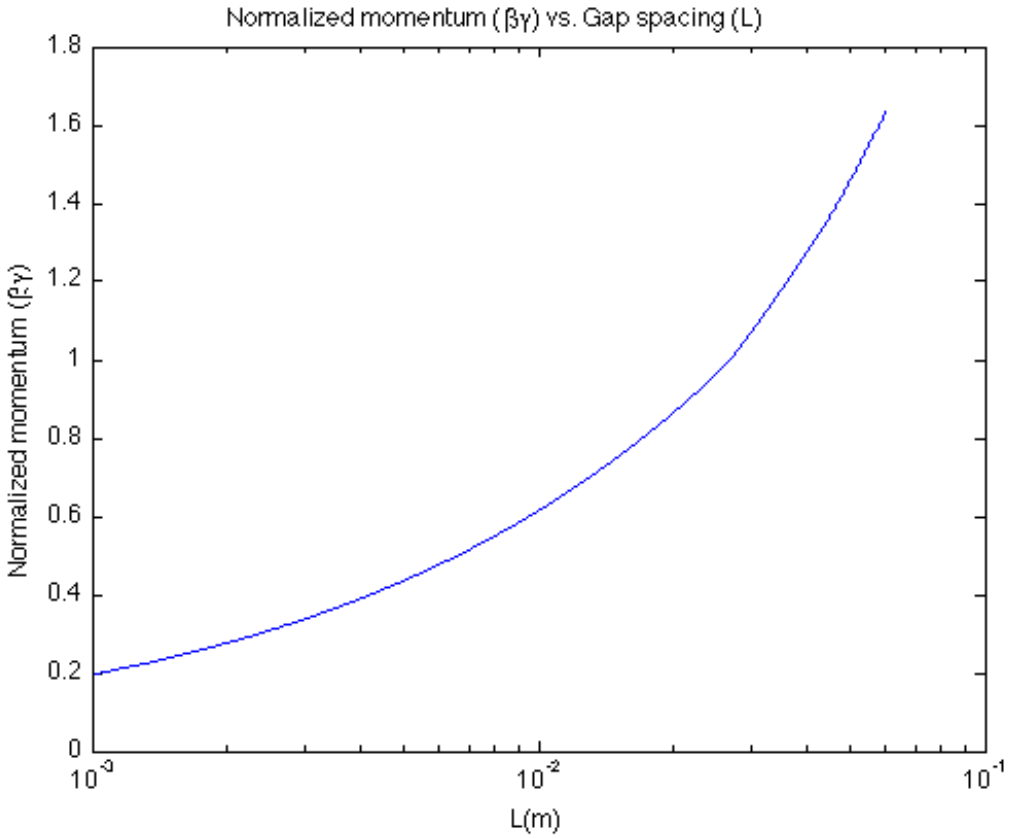

Figure 28. Average energy vs. gap spacing between the cathode and anode with a non-uniform electric field

Now that the "Beam Code" program is complete, we can use our determined operating points as inputs to Spiffe.

The "Beam Code" was designed to provide a rough approximation of configurations that should be acceptable for experimentation. This program runs quickly, and is easily modifiable for future cathode configurations. The Spiffe program is now used to take a more in-depth look at the 0.80cm test cell gap configuration. It will be able to

simulate additional effects, such as "space charge" forces, that the "Beam Code" does not take into account.

The cathode geometry was approximated and entered into Spiffe. Next, the electric field was applied to this cathode cavity, and as a function in Spiffe, it simulated field emission at the cathode surface. This simulation ran for approximately 2000 picoseconds (one RF period). The results were in relative agreement with the "Beam Code." Figure 29 shows the momentum profile of the beam at the output of the cathode-anode gap.

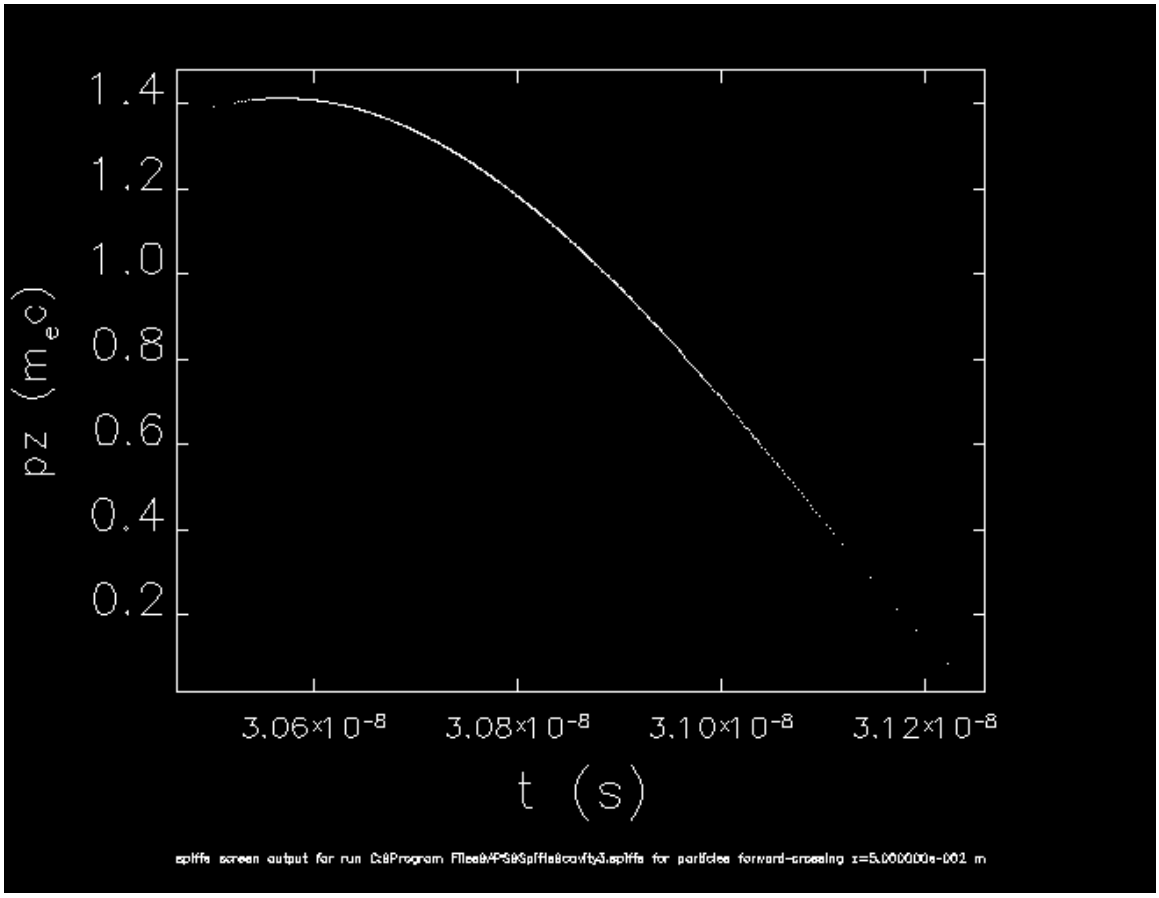

Figure 29. This is a graph of the electrons momentum as a function of time.

Figure 29 shows the momentum of the electrons along the z-axis as a function of time. The bulk of the beam appears to be bunched, but this is not very clear from this figure. Figures 30 and 31 are histograms constructed of the number of electrons as a function of time out of the gap (Figure 30), and a function of momentum along the z-axis (Figure 31). These two figures clearly show how the electrons are distributed with respect to time and energy for the test cell configuration.

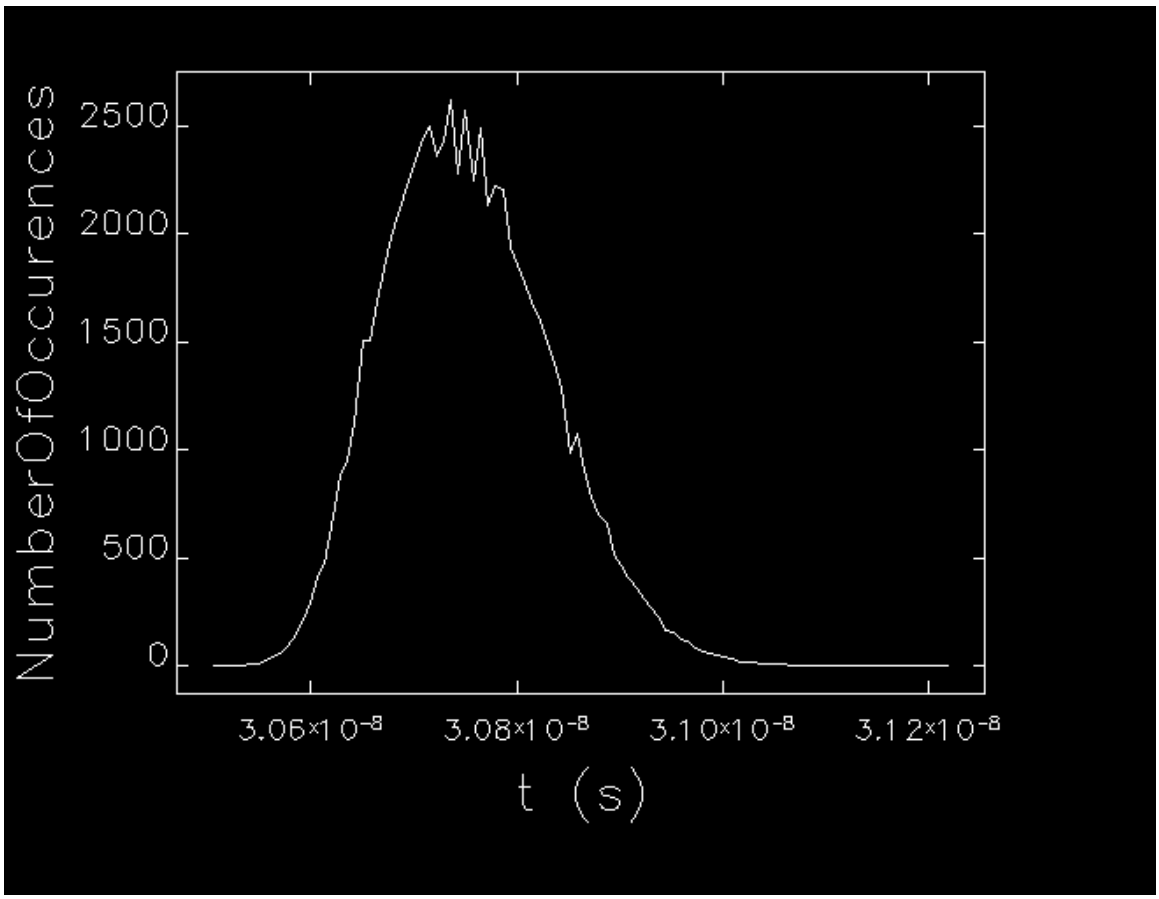

Figure 30. Histogram of the number of electrons as a function of the time to exist the cathode-anode gap.

In Figure 30, we can see that the electrons are bunched around a mean value of $3.075 \times 10^{-8}\,\text{sec}$ with a standard deviation of 79 picoseconds, which equates to a sigma of 14.75^{o}. Again, this is in relative agreement with the sigma used in the "Beam Code" of 10^{o}.

A useful feature of Spiffe is that all of the electrons simulated were launched with the same initial energy. Since each electron has the same energy, the number of electrons is analogous to the current density. Figure 31 relates current density to the energy of the electron beam.

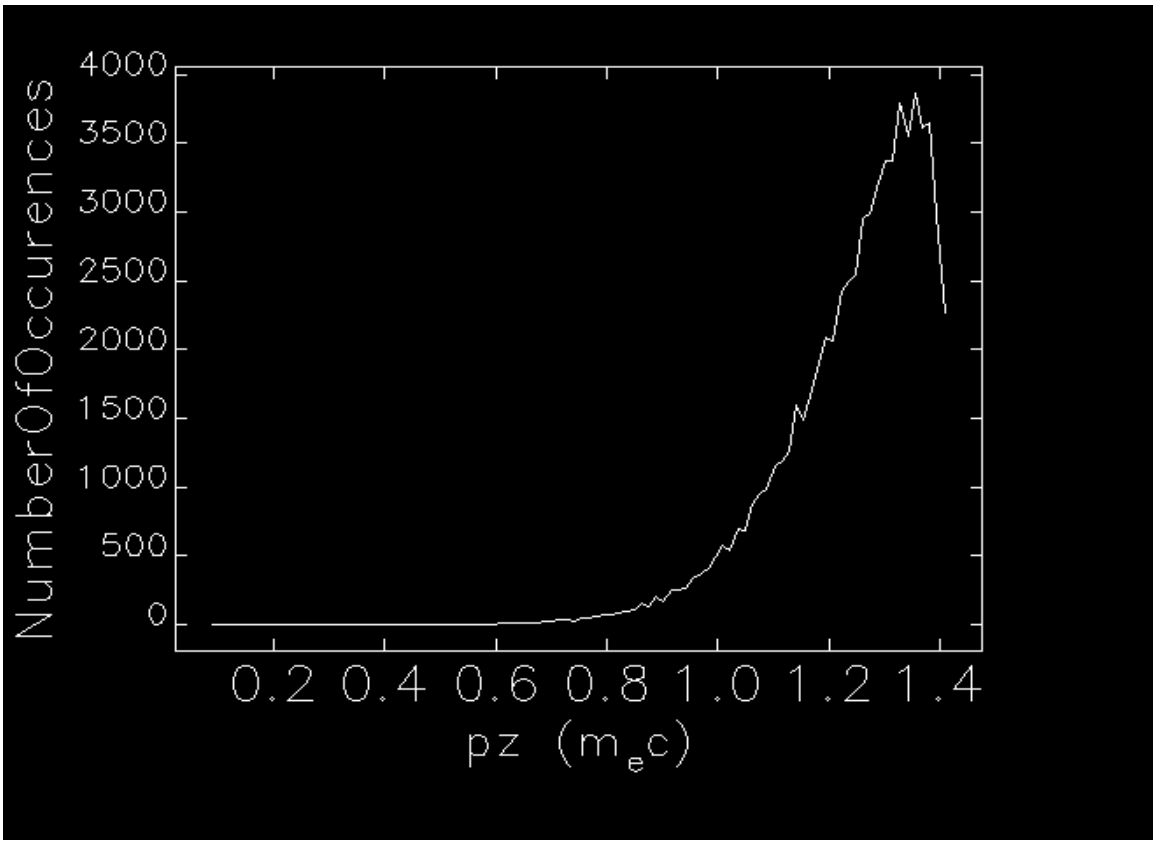

Figure 31. Histogram of the number of electrons as a function of momentum.

In Figure 31, the electrons have a RMS value of 1.25 and a standard deviation of 12.9%, which is acceptable for experimental purposes. It is important to note that this standard deviation is larger then the energy spread that was predicted in the "Beam Code" by approximately a factor of 7. However, this could easily be accounted for by the "space charge" forces, which are accounted for in the Spiffe program.

Figure 32 is a series of time "snap shots" of the beam as it travels through the cathode-anode gap.

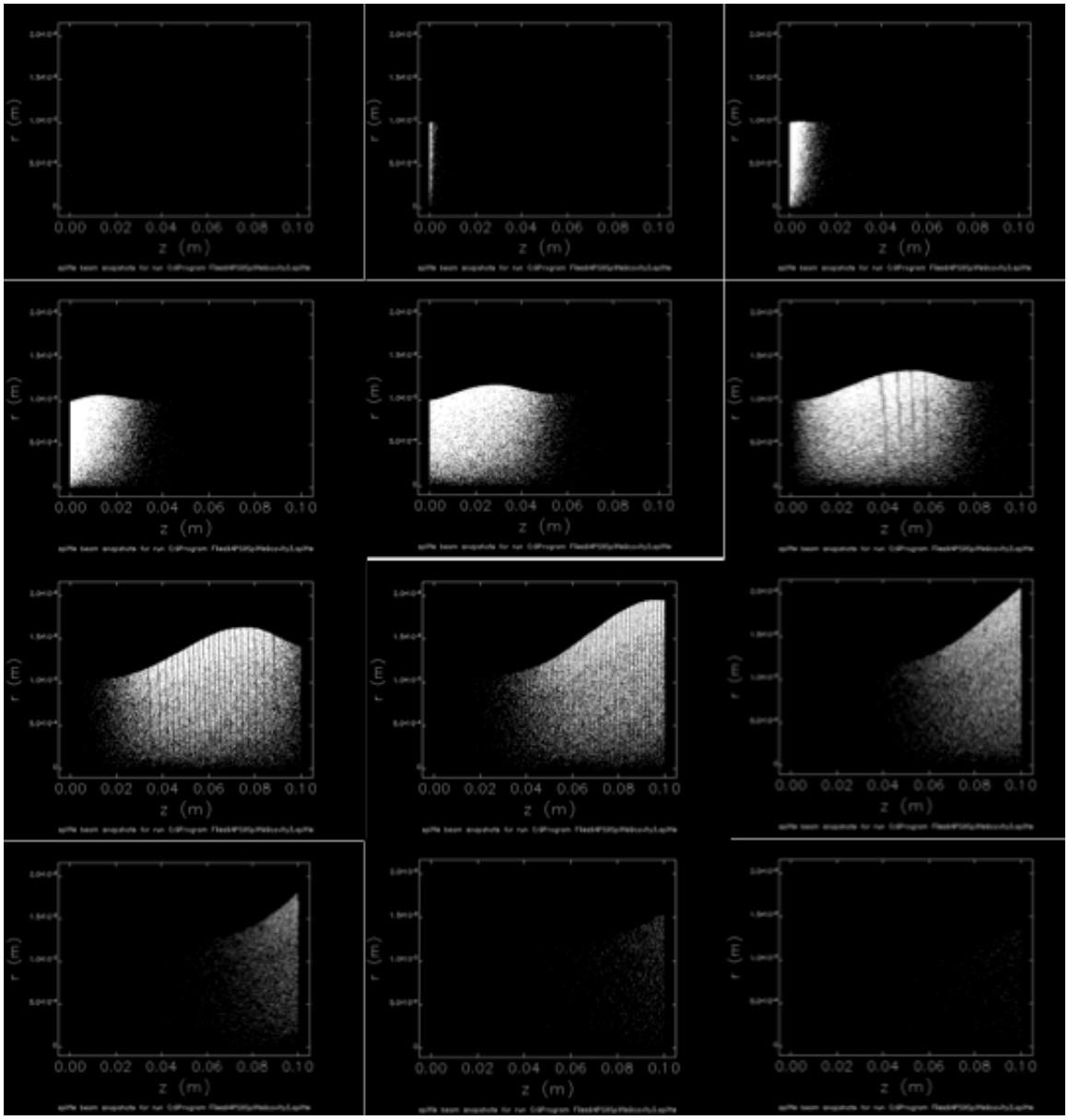

Figure 32. The electron beam progression through the cathode to anode gap. The vertical axis goes from the center of the cathode out to 2mm and the horizontal axis goes from 0 to 1cm for each slide.

Figure 32 follows the progression of the electron beam; the beam stays relatively intact with a 1.0mm increase in total beam radius. The results from the Spiffe simulations show that the designed cathode-anode geometry will be acceptable for further experimentation.

THIS PAGE INTENTIONALLY LEFT BLANK

VII. CONCLUSIONS

Based on the simulation results of the beam code and Spiffe simulations, the cathode-anode geometry and configuration are viable to be used in follow-on experimentation. The recommended initial gap spacing between the cathode and anode is 0.80cm. At this spacing, the DFEA should "turn on" with 100KV applied voltage. The phosphor screen will be able to provide a visual indication of the individual emitter tips that are producing electrons.

Because a high-voltage power supply is being used, there is the possibility that any surface irregularities could result in field emission. Thus, the test configuration should be energized for a period of time prior to the DFEA being installed. This will effectively condition the cathode test cell by vaporizing any field emission points on the cathode surface. Additionally, this will prevent the DFEA from damage should there be any arcing present when the system is initially energized. Once the cathode test cell is conditioned the DFEA can be installed and experimental results can be obtained.

It is also recommended that various gap spacings be tested, as the simulation results showed there is a range over which this geometry should work. The positioning motors that are attached to the anode assembly will allow for remote positioning adjustment. Therefore, adjustments can be made while the system is energized, so that the exact point at which the DFEA are activated can be determined. Also, the associated diagnostics will be

providing real-time feedback, which can be used to find the optimal point at which to operate this cathode-anode configuration.

Potential follow-on experiments could be to enclose the output from the anode in another accelerator cavity. In doing so, this accelerator cavity could further increase the speed of the free electrons and adjust their phase in order to further control the input electron beam for the FEL system.

APPENDIX BEAM CODE

A. BEAM CODE

```
/*
 *  thesis.c
 *
 *
 *  Created by Sam Hallock on 2/22/10.
 *  Thesis
 *
 */

#include<stdio.h>
#include<math.h>
#include<stdlib.h>
#define PI 3.14159

int main (void)
{

     float phi, dt, q, m, c, E, Eo, Fr, lambda, freq, alpha, L, Vo, p,
t, z, BG;
     float V, J, tout, tf, Espread, Jsum, BGJ, Inner, SigmaE, BGJ2;
     float Q[1000000];
     int i,D,w;
     FILE *output;
     output = fopen("thesis.txt", "w");
     FILE *outputb;
     outputb = fopen("thesis2.txt", "w");
     FILE *outputc;
     outputc = fopen("thesis3.txt", "w");
     Eo = 20*pow(10,6);
     Fr = 1;
     q = 1.602*pow(10,-19);

     c = 3*pow(10,8);
     m = 9.096*pow(10,-31);
     freq = 500*pow(10,6);

     dt = 1*pow(10,-13);
     alpha = 1.0;
     lambda = c/freq;
     D=0;

     for(L=0.001;L<0.06;L=L+0.00001){
     i=0;
     Inner = 0.0;
     Jsum=0.0;
      BGJ=0.0;
      Espread=0.0;
     for(phi=0.0;phi<PI;phi=phi+PI/100.0){
      z = 0.0;
      BG = 0.0;
      tout=0.0;

      J=exp(-1*((phi-PI/2)/(2*10*PI/180)*(phi-PI/2)/(2*10*PI/180)));

      for(t=0.0; t<1*pow(10,-9); t=t+dt){
```

```
            E = (Eo*Fr*sin(2*PI*freq*t+phi))*(1-z/L);
            z = z +c*BG*dt/sqrt(1+abs((BG)*(BG)));
            tf=t;


            tout=tf+phi/(2*PI*freq);
            if(z>L){
                  E=0.0;
                  t=1*pow(10,-9);

            }
            if(z<0.0){
                  E=0.0;
                  tf = t;
                  t=1*pow(10,-9);

            }
            BG = BG +(q/(m*c))*E*dt;

            }
      Jsum=Jsum+J;
            BGJ=BGJ+BG*J;
                  fprintf(outputb, "%E \t %E \t %E \t %E \t %E \t %E
\n", phi, tf, tout, BG, J, z);

      BGJ2=BG*J;
      Q[i]=BGJ2;

      fprintf(outputc,"%f \t %f \t %f \t %f \t %f\n", Q[i],BGJ2, BGJ,
BG, J);
      i=i+1;
      D=D+1;
     }
     Espread=BGJ/Jsum;

     for(w=0;w<i;w=w+1){
      //printf("Q[] %f \t Espread %f \n", Q[w], Espread);
      Inner = Inner +(pow(Q[w]-Espread,2));

            }
      //printf("Inner %f \n", Inner);
     SigmaE=sqrt(Inner/D);
     //printf("Counter %d \t Espread %f \t SigmaE %f BGJ %f \t Jsum %f
\t Inner %f \n", i, Espread, SigmaE, BGJ, Jsum, Inner);
     fprintf(output, "%d \t %E \t %E \t %E \n", D, Espread, SigmaE, L);


}
      fclose(output);
     fclose(outputb);
     fclose(outputc);
     return(0);
}
```

B. DEFINITIONS, RELATIONSHIPS, AND FORMULAS

Definitions

c (speed of light)
$\vec{r}$ (particle position)
$\vec{v}$ (particle velocity)
$\beta = \frac{v}{c}$ (normalized particle velocity)
$\gamma = \frac{1}{(1-\beta^2)^{1/2}}$ (Lorentz Factor)
$\vec{P} = \gamma mv = \beta\gamma mc$ (particle momentum)
$p = \frac{\vec{P}}{mc} = \beta\gamma$ (normalized momentum)
$E = \gamma mc^2$ (total particle energy)
KE = $(\gamma\text{-}1)mc^2$ (particle kinetic energy)
$\vec{E}$ (Electric field)
$\vec{B}$ (Magnetic field)

Relationships

$$\vec{P} = \beta\gamma mc = \frac{1}{c}(E^2 - m^2c^4)^{1/2}$$

$$\beta\gamma = \sqrt{\gamma^2 - 1}$$

$$\gamma = \sqrt{p^2 + 1}$$

$$\vec{v} = \frac{pc}{\sqrt{p^2+1}} = \frac{pc}{\gamma}$$

Relativistic Equations of Motion

$F = q\cdot(\vec{E} + v\times\vec{B})$ $F = \frac{d}{dt}\vec{P}$, $\vec{E}$ and $\vec{B}$ are functions of space and time

$$\frac{d}{dt}\vec{r} = \beta\cdot c \quad \text{---->} \quad \frac{d}{dr}\vec{r} = \frac{\vec{P}\cdot c}{\sqrt{m^2c^2 + p^2}} = c\cdot\frac{p}{\sqrt{1+(|p|)^2}} = \frac{c\cdot p}{\gamma}$$

$$\frac{d}{dt}p = \frac{q}{mc}(\vec{E} + c\cdot\beta\times\vec{B}) = \frac{q}{mc}(\vec{E} + c\cdot\frac{p}{\gamma}\times\vec{B})$$

THIS PAGE INTENTIONALLY LEFT BLANK

LIST OF REFERENCES

[1] William B. Colson. "PH 4911-Simulation of Physical and Weapon Systems," class notes, Winter 2010.

[2] "Free Electron Laser." Wikipedia, http:en.wikipedia.org/Free electron laser (January 2010).

[3] "Field Electron Emission." Wikipedia, http//en.wikipedia.org/wiki/field_electron_emission (January 2010).

[4] S.T. Pai and Oi Zhang, "Introduction to High Power Pulse Technology. *World Scientific* (1995).

[5] R.L. Edmonson "Free Electron Laser Stability Effects and Design of an Electrostatic cathode Test cell." Naval Postgraduate School (2009).

[6] C.L. Stewart, "Thesis: Measurement of Energy Spectrum of Electrons Field-Emitted from Diamond Field-Emitter Arrays." Vanderbilt University (2009).

[7] R.A. Neuerman "Simulation and Design Methods for Free-Electron Laser Systems." Naval Postgraduate School (2009).

[8] J.D. Jarvis, H. L. Andrews, C. A. Brau, B.K Choi, J. Davidson, W. Kang, S. Raina, S. M. Wong, "Development of Diamond Field-Emitter Arrays for Free-Electron Lasers." Proceedings of FEL08, Gyeongju, Korea (2008).

[9] J.D. Jarvis, & Andrews, H. L. & Brau, C.A., "Transverse Emittance of Diamond Field-Emitter Arrays". Proceedings of FEL08, Gyeongju, Korea (2008).

[10] Poisson Superfish (Version 7) [Computer software]. Los Alamos, NM: Los Alamos National Laboratory.

[11] Solidworks (Version SP5.0) [Computer software]. Concord, MA: Dassault Systèmes SolidWorks Corp.

[12] Spiffe (Version 3.2) [Computer software]. Argonne, IL: Argonne National Laboratory.

[13] J.W. Lewellen, J. Noonan, “Field-emission cathode gating for RF electron guns.” Physical Review Special Topics—Accelerators and Beams 8, (2005).

INITIAL DISTRIBUTION LIST

1. Defense Technical Information Center
   Ft. Belvoir, Virginia

2. Dudley Knox Library
   Naval Postgraduate School
   Monterey, California